AWAKEN Wind Plant Simulation Comparison

AWAKEN Simulation Group
April 14, 2023

Lawrence Cheung[1], Alan Hsieh[2], Myra Blaylock[1], Thomas Herges[2], Nathaniel deVelder[2], Kenneth Brown[2], Philip Sakievich[2], Daniel Houck[2], and David Maniaci[2], Colleen Kaul[3], Raj Rai[3], Nicholas Hamilton[4], Alex Rybchuk[4], Ryan Scott[4], Regis Thedin[4], William Radünz[5]

[1] Sandia National Laboratories, Livermore CA 94550, USA
[2] Sandia National Laboratories, Albuquerque, NM 87185, USA
[3] Pacific Northwest National Laboratories, Richland WA 99354, USA
[4] National Renewable Energy Laboratory, Golden, CO 80401, USA
[5] University of São Paulo, State of São Paulo, Brazil

Executive Summary

A series of numerical simulations of wind farms, using different model fidelities and for different atmospheric stability conditions, were performed as a part of the American WAKE ExperimeNt. The simulations included using FLORIS wake models, a number of microscale AMR-Wind and Nalu-Wind runs, as well as idealized and complex terrain WRF runs. The largest computations used the AMR-Wind LES solver to simulate a 100 km × 100 km domain containing 541 turbines under unstable atmospheric conditions matching previous measurements, while other LES computations focused on sections of the King Plains wind farm. Results of this qualitative comparison illustrate the interactions with wind farms with large-scale ABL structures in the flow, as well as the extent of downstream wake penetration in the flow and blockage effects around wind farms.

Introduction

The AWAKEN field campaign is currently underway, with measurements being actively gathered in the field and simulations being conducted. This report summarizes the progress of the AWAKEN Simulation Group towards successfully achieving the Q2 milestone and also laying the groundwork for the Q4 milestone.

Milestone Definition:

WETO.1.3.4.404, Q2: Complete simulations using the ExaWind Code suite, Nalu-Wind and AMR-Wind with ADM, of King Plains wind farm for a stable and unstable ABL condition. These simulations will be compared to simulation results from FLORIS and WRF-LES including terrain

effects. They will also inform possible instrument adjustment if, in the simulation, current instrument locations are deemed insufficient to test critical testable hypotheses.

Q2 Go/No-Go: Using gathered observations, determine if existing sites and operational strategies are sufficient to meet observation needs to address science goals. Suggest alternate operations and/or locations for instruments if needed.

AWAKEN Science Goals

While we prioritized addressing the Q2 milestone, the simulations conducted here were all done in the context of the broader AWAKEN testable hypotheses

1. Wind farm wakes depend on atmospheric and operating conditions and impact regional wind power production.
2. Wind turbines in the interior of wind farms tend to encounter more turbulence. Wind farm blockage depends on atmospheric and operating conditions
3. Wind farm control benefits large farms. The maximum energy extracted by a wind plant is constrained by the momentum flux between the surrounding atmosphere and the wind farm
4. Turbine wakes are impacted by stochastic events
5. Dynamic intermittent turbulent events (bursting, gravity waves, K-H instabilities, etc.) lead to power fluctuations in wind farm power production

In the Q2 update, the Simulation Group prioritized analysis that addressed hypotheses 1, 2, and 3. We conduct simulations in both stable, unstable, and neutral conditions that are representative of the climatology at the AWAKEN site using a variety of codes (AMR-Wind, FLORIS, Nalu-Wind, WRF). All of the code-to-code comparisons rely on enforcing similar conditions at the large-scale across all simulations.

Case Study Description

Atmospheric Conditions

The conditions for the numerical simulations are derived from measurements at the nearby Atmospheric Radiation Measurement (ARM) Southern Great Plains facility. Table 2 shows the data taken at the ARM Central Facility (site C1) and includes wind speed, turbulence, and shear information collected from Jan. 2015 to Nov. 2020. In all cases, the primary wind direction was 175±10 degrees. Data corresponding to unstable, near-neutral, and stable conditions was available, although the current study focuses on simulations of the unstable and stable atmospheric boundary layer (ABL), while simulation results for the neutral case will appear in future work.

Table 1: Atmospheric boundary layer parameter values for each study case.

Parameter	Unstable ABL	Stable ABL	Neutral ABL
Wind Speed at 91 m [m/s]	9.0	10.1	11.35
Wind Shear Exponent	0.09	0.32	0.167
Potential Temp at 3 m [K]	305.8	302.3	301.84
Friction Velocity [m/s]	0.49	0.32	0.5349
Turbulence Intensity at 60 m [%]	18	9.6	14.85

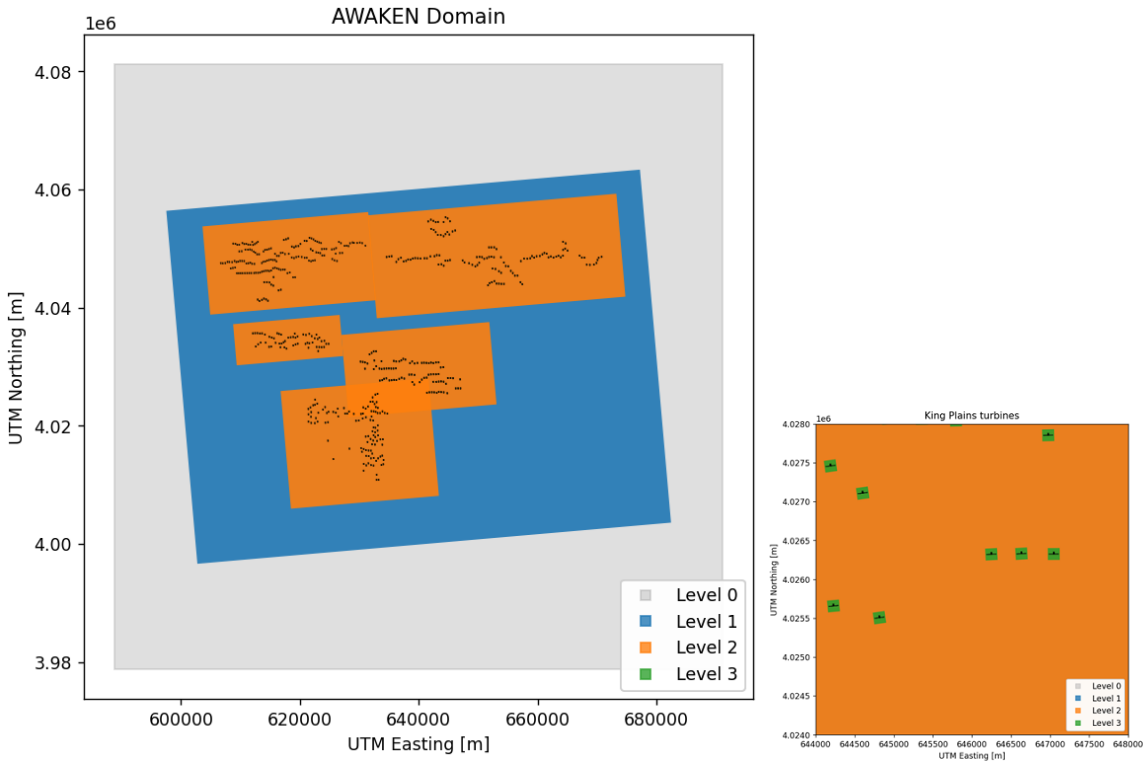

Figure 1. Largest domain used for the unstable ABL run on Summit with all five wind plants. The colors indicate the grid spacing, going from coarsest surrounding the plants to the finest closest to each turbine.

Model Comparisons

A summary of the different simulations performed as a part of this milestone is provided in Table 2. The major focus for many of the simulations was the eastern section of the King Plains wind farm, which corresponds to the location of several planned AWAKEN lidar and turbine instrumentation sites. The AMR-Wind and Nalu-Wind simulations covered both the unstable and the stable ABL conditions, while the FLORIS TurbOPark model was able to simulate all three stability states.

Table 2: Simulations applied to each study case in the current report.

Unstable	AMR-Wind (All 5 wind farms) AMR-Wind (Eastern section of King Plains) Nalu-Wind (Eastern section of King Plains) Nalu-Wind (Eastern section of Thunder Ranch) WRF (Eastern section of King Plains), both with and without terrain FLORIS-TurbOPark (All 5 wind farms) FLORIS-Gaussian Curl (entire King Plains)
Stable	AMR-Wind (Eastern section of King Plains) Nalu-Wind (Eastern section of King Plains) FLORIS-TurbOPark (All 5 wind farms)
Neutral	FLORIS-TurbOPark (All 5 wind farms)

Note that for simulations which include Armadillo Flats, only turbines which were available within the US wind turbine database and operator databases at the time of the simulation setup were included. There are several recently added turbines to the Armadillo Flats layout which are not included in these simulations.

Turbine Representation

To lower the computational expense of the LES and to keep the models consistent between different simulations types, all studies for this milestone used actuator disk models (ADM) to represent the turbine dynamics. An OpenFAST model for each of the turbines in the study area was developed by scaling publicly available reference turbines such as the IEA 3.4-130. No proprietary wind plant or turbine data were used in the simulations. The scaled models were tuned to match the correct hub height, rotor size, and power rating with reasonable approximations of the thrust behavior.

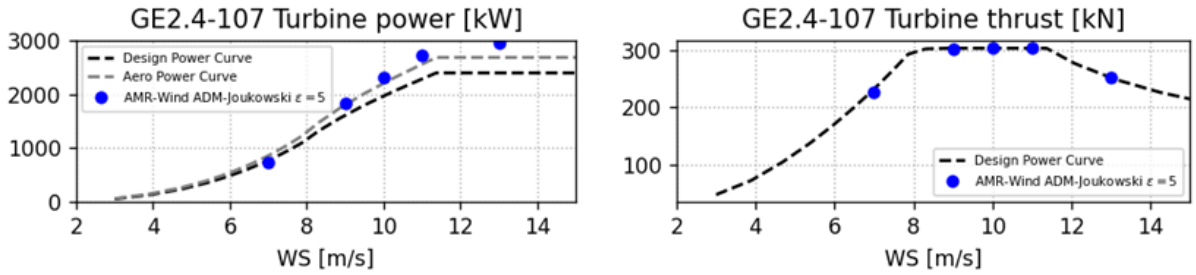

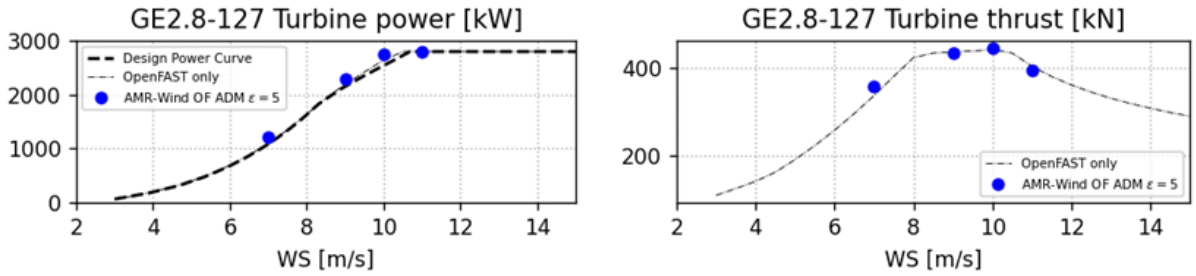

Figure 2. Power and thrust curves for two of the turbines used in the simulations with OpenFAST models.

For the AMR-Wind and Nalu-Wind calculations, the actuator disc model parameterization also underwent a calibration process to accurately match the target power and thrust behavior. The calibration simulations were run in AMR-Wind on a smaller domain with a single turbine, represented using the ADM-Joukowski or ADM-OpenFAST model, placed in the center; three levels of mesh refinement were used to match the primary multi-farm simulations. As shown in the figure above, the power and thrust predictions from the calibration simulations were compared with the design curves of the respective turbines. Parameters such as the size of the isotropic smoothing kernel and the vortex core size in the Joukowski model were adjusted until the agreement was satisfactory for the wind speeds of interest.

In the Nalu-Wind simulations of the King Plains and Thunder Ranch wind farm subsets, the ADM-OpenFAST coupled model was used for the GE 2.8-127 and GE 2.5-116 turbines, respectively. AMR-Wind calculations also used the ADM-OpenFAST coupled model for the GE 2.8-127 turbines at the King Plains wind farm. However, for the largest scale AMR-Wind simulation with all wind farms, the ADM-Joukowski model was used for the other wind farms (Armadillo Flats, Breckinridge, Chisholm View, and Thunder Ranch).

Simulation Code Descriptions

AMR-Wind

AMR-Wind (Sprague, 2020) solves the incompressible Navier-Stokes equations with variable density and viscosity. Additionally, scalar transport equations can be solved, such as potential temperature or turbulent kinetic energy. The discretization in AMR-Wind is based on the approximate projection method used in IAMR (Almgren, 1998) and incflo (Sverdrup, 2018). It is a semi-staggered scheme where the velocity and scalar variables are located at cell centers and pressure is located at nodes. Pressure is also staggered in time so that pressure and the pressure gradient are at time n+1/2. The time discretization is handled with a Crank Nicolson approach, and the advection term is handled explicitly using an upwind finite-volume method using the WENO-Z algorithm. The diffusion terms can be handled explicitly, semi-implicitly, or implicitly and are spatially discretized using a second-order central difference formula. For the simulations in this paper, we use an implicit scheme for the viscous terms, as the variable viscosity from the eddy viscosity may cause time step restrictions. After the scalar equations

and the momentum equations are advanced in time, a nodal projection is used to approximately correct the velocity field to make it divergence free.

In all simulations with AMR-Wind, both the Coriolis forcing and Boussinesq buoyancy model were included to capture the effects of wind veer and atmospheric stratification. The subgrid-scale kinetic energy one-equation turbulence model was employed to close the large eddy simulation (LES) equations. At the lower boundary, the sub-filter scale stresses are applied following the formulation of (Moeng, 1984). A temperature inversion was also applied at z = 1500 m to limit the growth of the ABL in the vertical direction.

The wind farm simulations performed in this study were carried out in a two-stage process. In the first stage, a precursor calculation is used to develop the correct ABL inflow boundary conditions. The precursor calculation used an ABL forcing scheme where a constructed pressure gradient was applied to ensure that the hub-height wind speed at z = 91 m matched the ARM measurements, and horizontally periodic boundary conditions were used. To arrive at the correct shear and turbulence intensity characteristics, two wall model parameters were varied at the ground: the surface roughness $z0$ and the applied temperature gradient at the ground. Future simulations will also explore the use of inflow velocity and temperature forcing derived from idealized mesoscale WRF simulations.

Once the appropriate ABL conditions are established, the second stage of the simulation uses the precursor solution as the initial condition and the saved boundary data as the inflow conditions. These calculations include additional mesh refinement and turbine models to capture the full operation of the AWAKEN wind farms.

For the largest unstable ABL simulation of the AWAKEN wind farm site, a 100 km × 100 km × 2.5 km domain was used which included all five wind farms of interest (see Figure 1). The background mesh resolution (level 0) was 20 m × 20 m × 20 m and was successively refined to achieve 2.5 m × 2.5 m × 2.5 m mesh resolution (level 3) surrounding the turbine rotor regions. For the simulations that included the turbine models, the total mesh size was 21.14B elements,. Simulations were run on 6000 GPUs on the Summit high-performance computing system at Oak Ridge Leadership Computing Facility, and have used approximately 1 million GPU-hours to this point.

Nalu-Wind

The multiphysics, massively parallel code Nalu-Wind (Sprague et al., 2020; Domino, 2015) performs LES of the ABL, using a node-centered finite volume discretization to solve the acoustically incompressible Navier-Stokes equations with an approximate pressure projection technique, and a one equation, constant coefficient, turbulent kinetic energy model for the subgrid scale stresses (Yoshizawa et al., 1985). A wall function based on Monin-Obukhov theory is used for the bottom boundary and an inflow/outflow boundary condition is used at the top (Vasaturo et al., 2018). The inflow/outflow condition uses a potential flow solution in wavenumber space which dampens high-frequency disturbances at the upper boundary. The

boundary condition on the domain sides is periodic. The flow solver is coupled to an appropriate OpenFAST model for each turbine (https://nwtc.nrel.gov/OpenFAST).

ABL forcing source terms are provided to the momentum equation to drive the flow to a predetermined velocity at a specific height, where the force is proportional to the difference between the desired spatial averaged velocity and the horizontally averaged instantaneous velocity. Similar to AMR-Wind, a two-stage process using a precursor calculation to develop the correct inflow boundary conditions and then a turbine calculation that uses the precursor solution data for both the initial flow field and inflow conditions. The wall model parameters of surface roughness z0 and the surface heat flux at the ground were also calibrated to arrive at the correct shear and turbulence intensity characteristics. Coriolis forces are also taken into account.

Unstable and stable ABL simulations using Nalu-Wind were performed for the King Plains wind farm. A 9.5 km x 9.5 km x 0.8 km domain was used for the stable ABL case and a 20 km x 20 km x 2.5 km domain was used for the unstable ABL case. The background mesh resolution was 20 m and 10 m for the unstable and stable cases, respectively, and were successively refined to achieve 2.5 m mesh resolution around the individual turbines. The total mesh sizes for the unstable and stable cases were 258 million and 245 million elements, respectively. The unstable and stable ABL cases simulated 41 and 31 turbines respectively, as the stable case did not incorporate a back row of ten turbines in King Plains that was simulated in the unstable case.

Idealized WRF

The characteristic shape and size of coherent structures in a simulated wind field vary depending on the surface and lateral forcing conditions used in the simulation. For example, for different combinations of surface heat flux and mean wind speed values, convective boundary layers transition between roll and cell type structures. The performance of wind farms could vary due to the interaction of different flow structures with the wind farm, so it is important to assess whether the forcing conditions provided to an LES model are realistic and, in turn, whether the LES simulates a realistic response of the flow to these forcings. Herein, we present the vertical and horizontal slices of wind speed and the vertical profiles of wind speed and potential temperature simulated by WRF for the cases: a) real-case simulation using High-Resolution Rapid Refresh (HRRR; https://rapidrefresh.noaa.gov/hrrr/) data as boundary and initial conditions (Case HRRR), b) idealized simulations that use the sounding of wind speed and temperature from Sonde profiles (case Sonde) for the same date as case HRRR, and c) idealized simulation that uses a composite convective profile of wind speed and temperature (Case Idealized). Case HRRR uses the HRRR data for boundary conditions in the outer domain, whereas the other two use doubly periodic boundary conditions in the outermost domain. Results presented here for all cases are derived from the innermost domain that has a horizontal grid spacing of 30 m and was obtained from performing simulations in the WRF framework. The case study date for Case HRRR and Case Sonde was selected to provide nominally similar conditions to Case Idealized.

Figure 3a-3c shows the wind speed contours in the vertical XZ plane up to the heights of 1.5 km for the three cases. The Case HRRR shows a heat flux of 350 W/m^2 on the surface and a wind speed of 7.8 m/s at z = 90 m above the surface. The Cases Sonde and idealized have the surface heat flux of 60 W/m^2 and 130 W/m^2 with a wind speed of 9 m/s at z = 90 m above the surface. The plane-averaged vertical profiles of wind speed and potential temperature (Figure 3d and 3e) of these cases also show the differences in their value because of different forcing functions used. The wind speed contour for the real case in Figure 3a clearly shows the updraft and downdraft of convective structures in the entire boundary layer depth of 1.5 km. The wind speed contour in the horizontal XY plane in Fig 3g for the real case also supports the existence of updraft and downdraft of air resulting from the larger surface heat flux. The wind speed contours of the vertical plane for the other two cases (Figure 3b-3c), however, show different flow structures than the real case. Their flow structures are smaller compared to the real case, and the contour of wind speed shows streak-like structures along the prevalent wind direction in the horizontal slice (Figure 3f). The results of various cases show that the flow structures could vary depending on the forcing conditions used in the simulations. This variation of the flow structures could significantly impact the performance of wind farms.

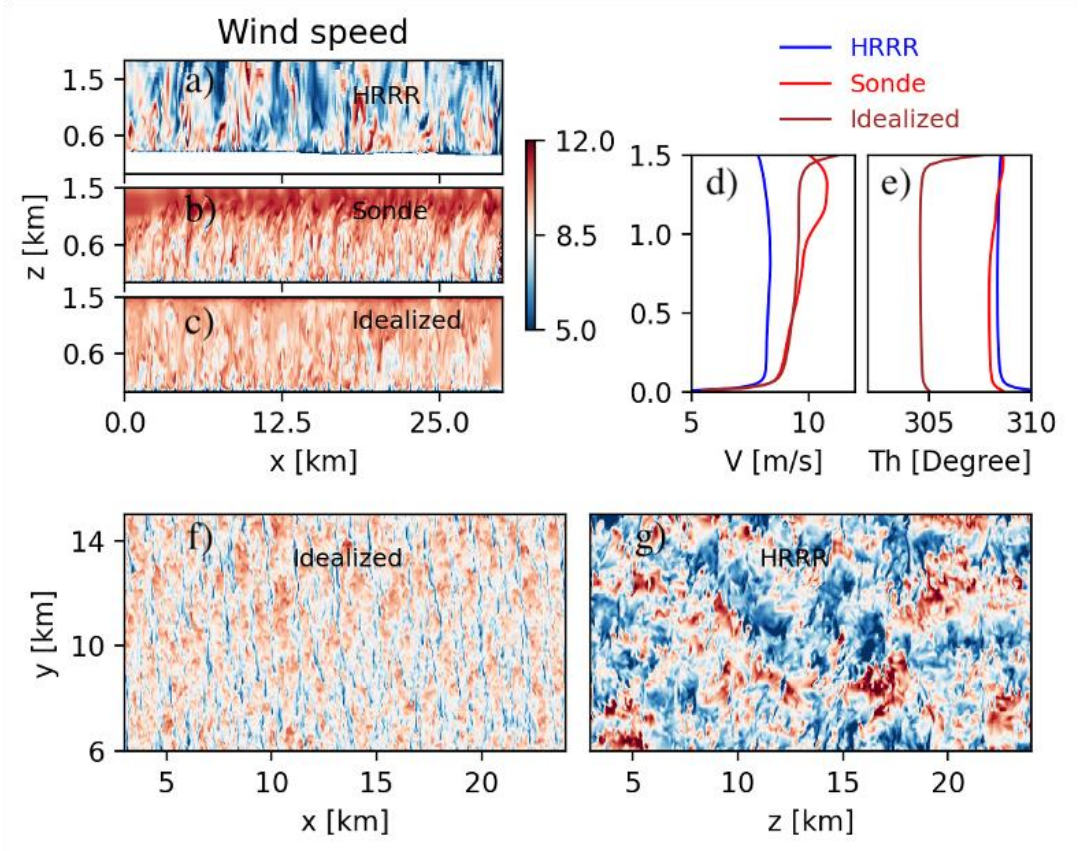

Figure 3. Wind speed examples for Idealized WRF simulations.

Idealized WRF-LES-GAD

The multi-scale simulations were performed with the Advanced-Research Weather Research and Forecasting (WRF) model version 4.1.5 (Skamarock *et al.*, 2019), which solves the compressible Euler equations for the three spatial dimensions and time. Several processes are included via parameterization schemes, such as for cloud formation physics, radiation, and the exchange of momentum, heat, and moisture with the land surface. The model is capable of running real forecasts for a selected region of the globe by using initial and boundary conditions derived from forecast systems or reanalysis products, such as ERA5. It can also run idealized simulations that are initialized with a user-specified dictionary containing vertical profiles of wind speed components, potential temperature, and moisture. In this report we used idealized simulations initialized by these user-specified profiles.

Two computational domains were used for the idealized simulations: a parent domain (D1) that uses periodic lateral boundary conditions and a nest domain (D2) with lateral boundary conditions specified and mapped from its parent. Both domains rely on WRF's large-eddy simulation (LES) capabilities and do not use planetary boundary layer (PBL) schemes. Thus, fine spatial resolutions of 100 m and 10 m were used. The D1 domain initializes with a constant wind speed of 14 m/s and direction of 190º based on trial and error. To reduce computational cost, the lower-resolution and cheaper domain D1 runs for 4 hours with the nest switched off to properly initialize turbulence and the desired boundary layer characteristics, in a fashion similar to that described in Idealized WRF. After 4 hr of spin-up time, the convective boundary layer and turbulence fully develop and reach an average hub-height wind speed of 9.4–9.6 m/s and a wind direction of about 170º. This will lead to higher power production. After the D1 is spun-up, the D2 domain is switched on and the wind farm simulation takes place from about 50 minutes. The sensible heat flux (52 W m^{-2}) and surface roughness (0.15 m) are matched to the AMR-Wind setup. To accelerate the development of fine-scale turbulence in the nest, the cell-perturbation method (CPM), which applies random perturbations to the potential temperature field, was employed across the boundary-layer (Muñoz-Esparza *et al.*, 2015).

Wind turbines are represented as generalized actuator disks (GAD) and implemented in the WRF code (Mirocha *et al.*, 2014). Based on the WRF-computed wind speeds at the actuator disk for each individual turbine and turbine control and blade-section aerodynamics properties, aerodynamic lift and drag forces are computed and projected on the actuator disks; these are accounted for in WRF's momentum tendencies. The current GAD implementation has a simple control mechanism that yaws the turbine toward the incoming wind direction. We implemented the NREL 2.8 MW turbine in WRF to better match the real GE 2.8 MW of King Plains. The GAD computes the raw aerodynamic power, which differs from the electric output of the real turbines. Thus, we have converted this raw aerodynamic power into output electric power by considering an efficiency of 90% and by limiting maximum power to the rated value (2.8 MW). An air density of 1.17 kg m^{-3} was adopted.

Several physical processes and their associated parameterization have been omitted from the simulations, such as moisture phase changes, cloud formation, and radiation. The Deardorff 1.5

TKE subgrid scale model was used for the LES (Deardorff, 1980) with the nonlinear backscatter and anisotropy (NBA) model (Kosovic, 1997). Four runs were performed in total: eastern King Plains with (case 1) and without turbines (case 2) considering a flat terrain, and eastern King Plains with (case 3) and without turbines (case 4) considering SRTM's ⅓ arc sec (~10 m) terrain elevation map within the innermost domain. The runs without turbines serve to isolate the turbine effects in the flow field.

Figure 5 illustrates the post-processed digital elevation model as used in the simulations. It was based on the SRTM's ⅓ arc sec database, which has a spatial resolution of about 10 m. It was necessary to smooth the original topography toward flat horizons and to set the latter as the zero level (0 m). Thus, there are negative heights in some areas. Some additional smoothing was employed to alleviate kinks in the resulting elevation map. The terrain was included in cases 3 and 4 only for the innermost D2 domain. The outermost domain D1 remained flat.

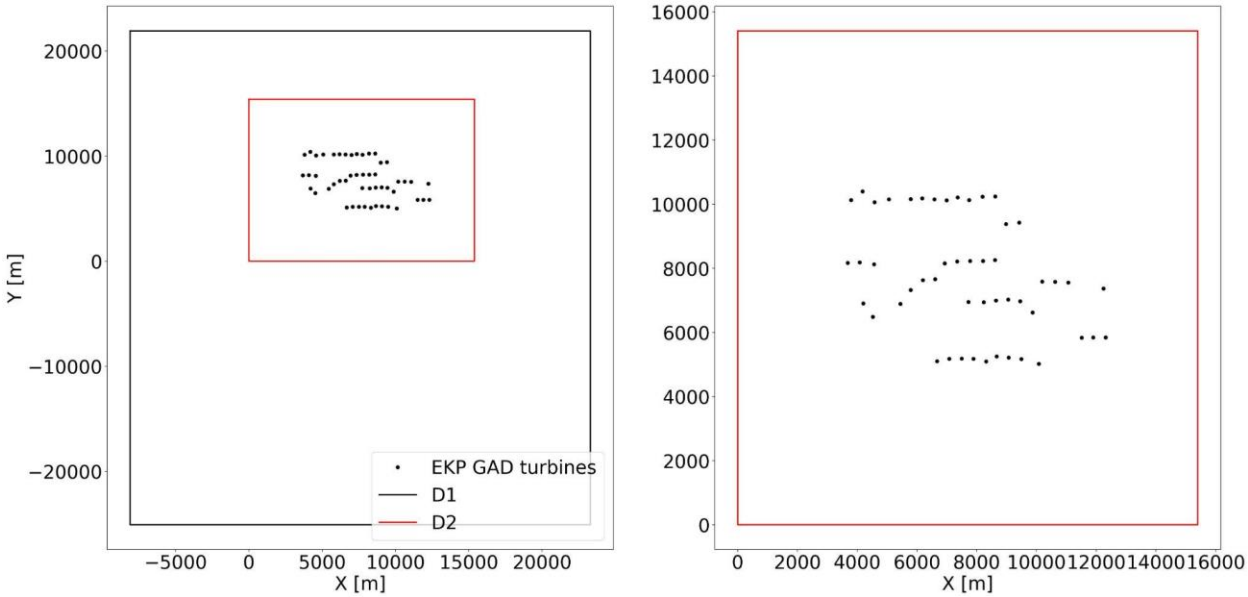

Figure 4. Computational domains employed in the idealized WRF-LES-GAD simulations for eastern King Plains consist of a parent (D1) and a nest (D2), whereby the GAD is represented only in the nest. The origin of the local coordinate system is the southwest corner of the D2 domain. A fifty-turbine subset of King Plains was selected for the simulations, similar to one of the AMR-Wind setups.

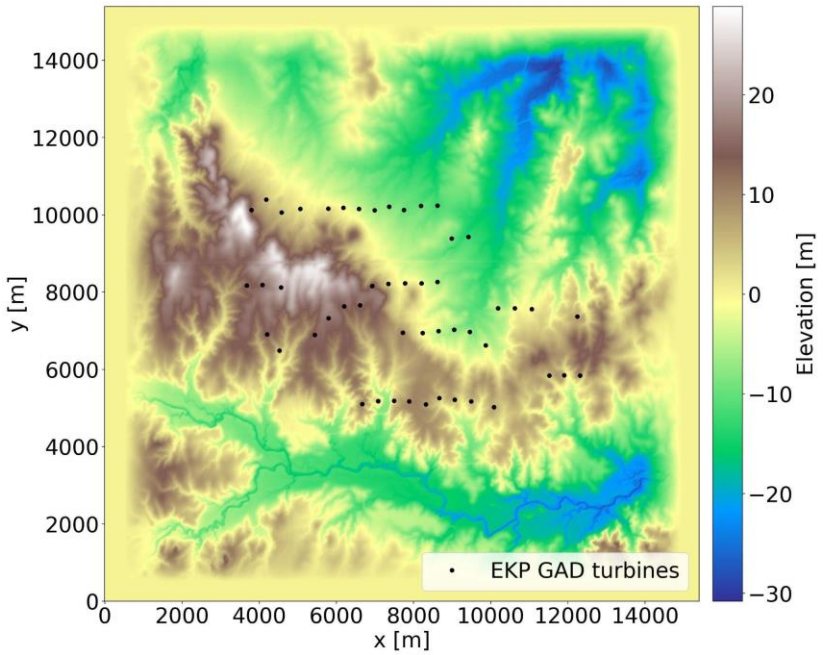

Figure 5. Post-processed digital elevation model employed for the D2 domain in the terrain cases (3 and 4).

FLORIS

Wind plant simulations were performed with the FLOw Redirection and Induction in Steady State (FLORIS) framework, version 3.1. Turbine models were created using WISDEM/WEIS and manually adjusted to match observed power from SCADA where possible. The TurbOPark model was selected for simulations of the complete AWAKEN system based on comparisons between the available models in FLORIS and measured turbine power. This model was designed to capture far wake expansions and has shown good agreement with measured plant performance in offshore settings. Model parameter tuning was achieved by minimizing the difference between FLORIS frequency-weighted mean power estimates and the frequency-weighted mean power measured at King Plains for each atmospheric condition. Optimal agreement between data sets was realized by increasing FLORIS turbulence intensity by a constant 2.5 % and setting the wake expansion parameter, A, to 0.2. Hub-height flow fields were obtained for King Plains with the Gauss-Curl Hybrid (GCH) model. The GCH model is designed to capture wake dynamics on the order of typical turbine spacing and includes the effects of secondary steering within the plant.

Simulation Comparisons

Background Flow and Inflow Characterization

A comparison of the horizontal velocity profiles at King Plains for the AMR-Wind, Nalu-Wind, and WFR-LES-GAD simulations shows the differences in the inflow velocities for the various solvers. For the unstable ABL condition, the averaged horizontal velocity inflow was computed at approximately 30D and 19D upstream of the first row turbines in the AMR-Wind and Nalu-Wind simulations, respectively. For the mesoscale WRF simulations, the inflow profile was taken at the first turbine row (0.0D upstream) itself. Both the AMR-Wind and Nalu-Wind profiles agree well, and match the desired hub-height inflow velocity (9 m/s) and also show similar shear across the rotor disk. However, for the WRF simulations, the inflow hub-height wind was larger, approximately 9.4 m/s for the flat case, leading to higher power predictions.

In the stable ABL case, both the AMR-Wind and Nalu-Wind inflow profiles agree well near the ground and at hub-height. However, note that a lower inversion height was used for the stable case in AMR-Wind compared to Nalu-Wind to help accelerate the convergence time of the larger domain. This led to some differences in the inflow velocity profiles above hub-height, although the shear profile still agreed reasonably well.

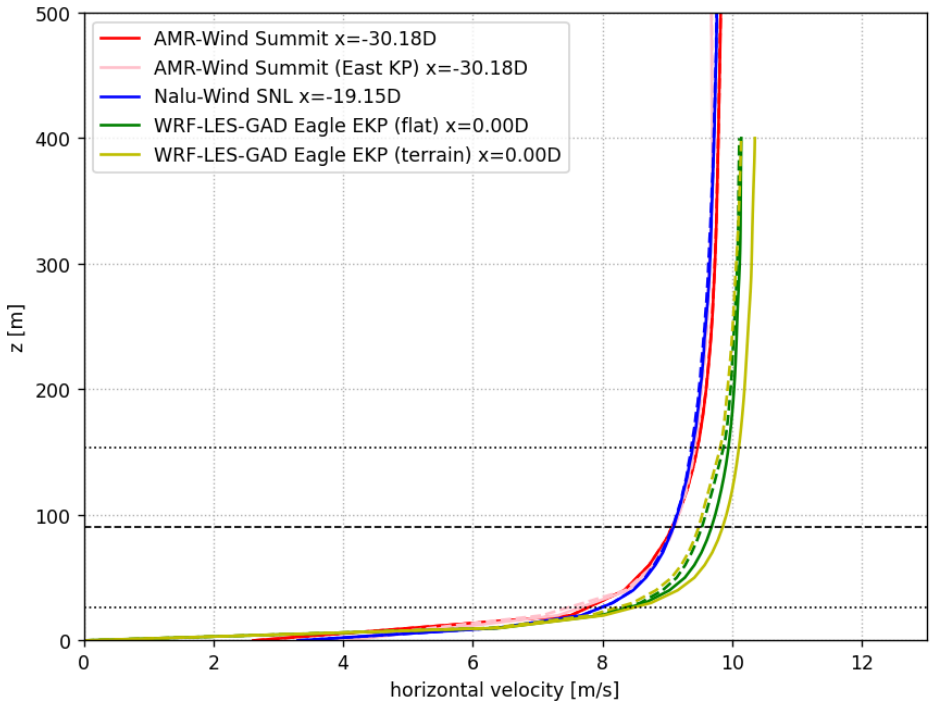

Figure 6. Horizontal velocity profile for incoming wind for the unstable ABL upstream of King Plains. Solid lines show precursor runs while dashed lines show runs that include turbines. The black dashed and dotted lines represent the turbine hub-height and rotor disk extents, respectively.

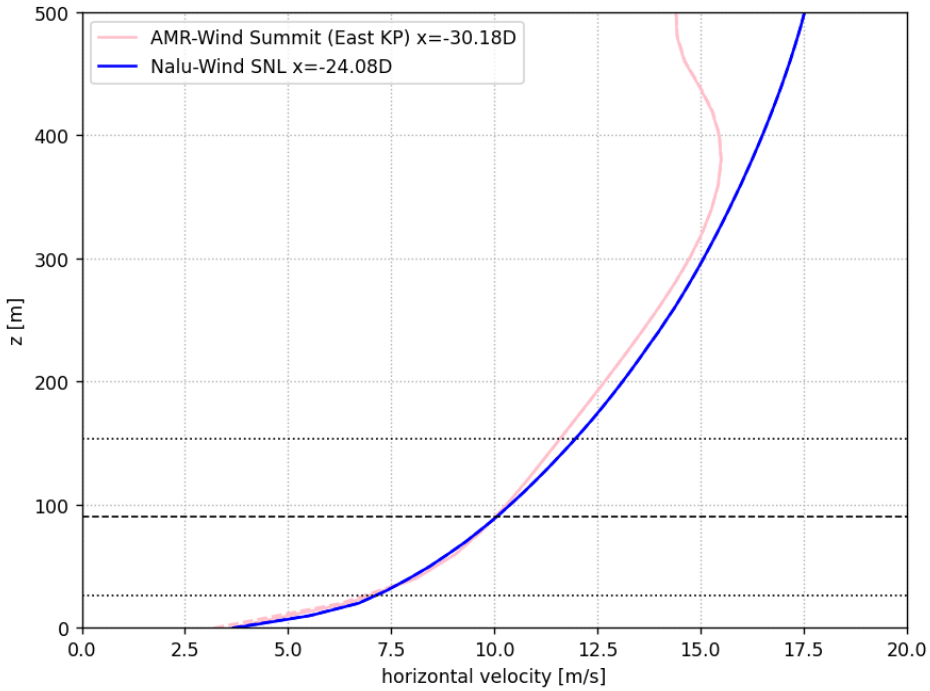

Figure 7. Horizontal velocity profile for incoming wind for the stable ABL.Solid lines show precursor runs while dashed lines show runs that include turbines. The black dashed and dotted lines represent the turbine hub-height and rotor disk extents, respectively.

Wind Turbine Power Production

A comparison of the power production from each of the simulated wind farms is shown in the figures below. In each case, the total power generated from the wind farm is divided by the number of turbines simulated to produce a turbine average. For the King Plains wind farm in the unstable ABL condition, the FLORIS TurbOPark and WRF simulations produced similar power, approximately 2.2MW per turbine, while the Nalu-Wind simulations predicted slightly less power. For the AMR-Wind King Plains simulations, the averaged power generation was less, approximately 1.9MW per turbine over the last 10 minutes of the simulations.

The comparison of averaged power output between the large scale AMR-Wind simulation and FLORIS TurbOPark model is also available for the Thunder Ranch, Armadillo Flats, Breckinridge, and Chisholm View wind farms for the unstable ABL condition as well. The results from the Nalu-Wind simulation for Thunder Ranch are included as well. For these wind farms, the averaged turbine power output agrees fairly well.

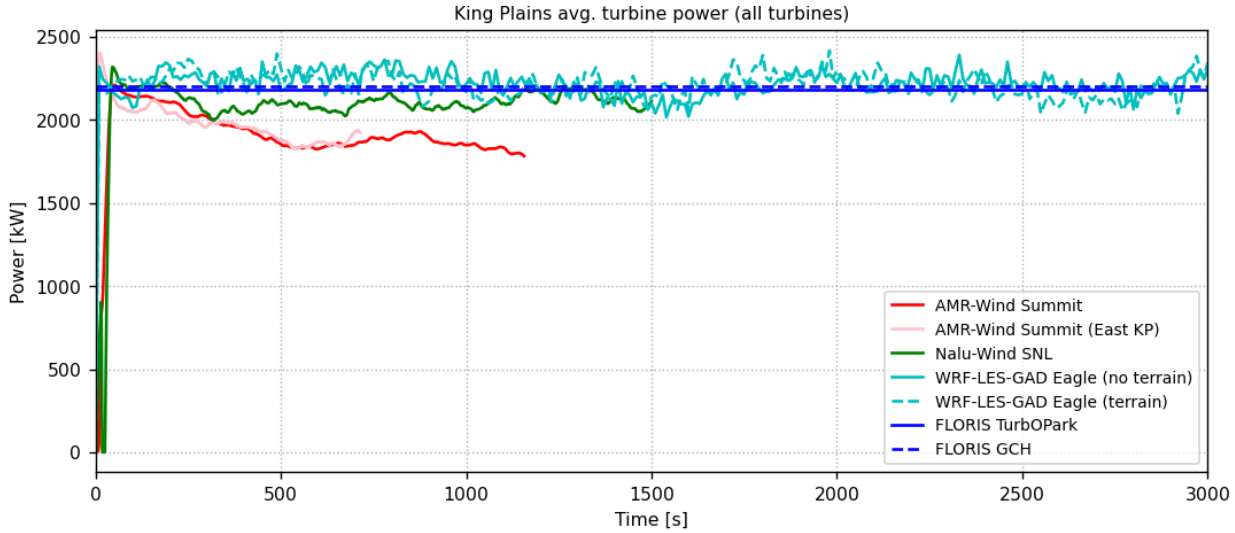

Figure 8. Average power for all turbines in each solver case for the King Plains wind plant with an unstable ABL. Each case might have a different number of turbines.

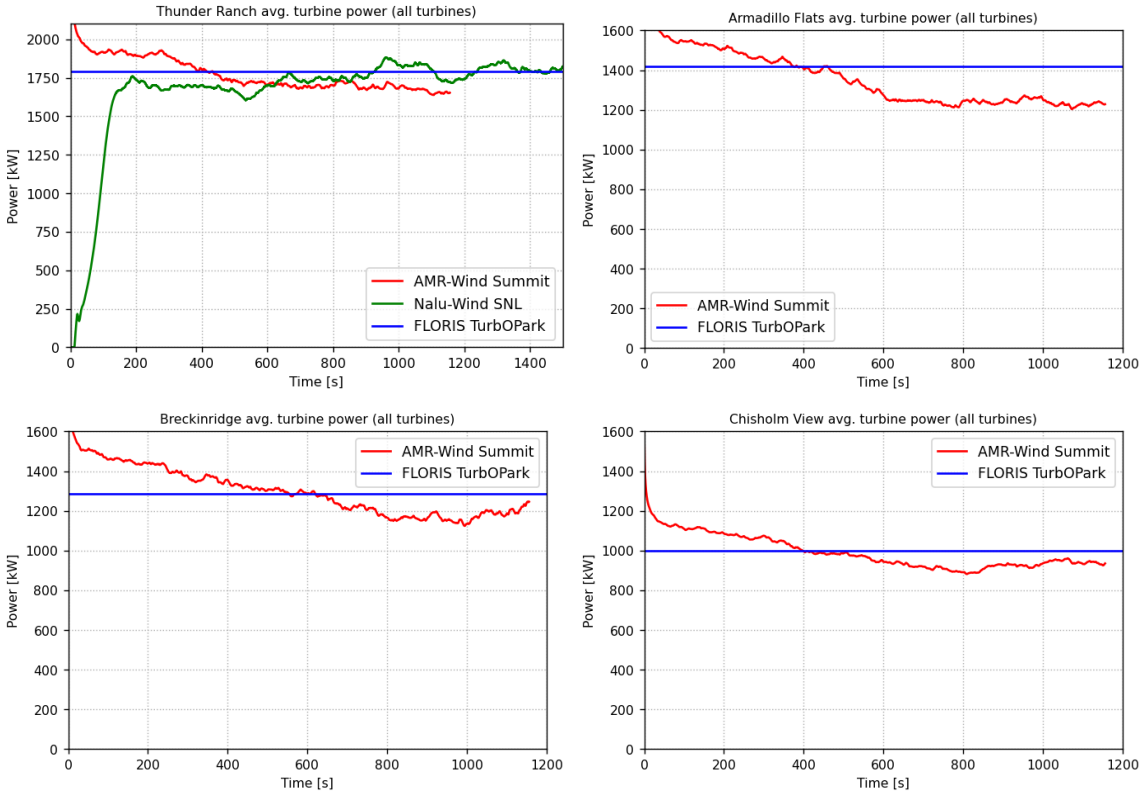

Figure 9. Average power for all turbines in each solver case for the Thunder Ranch, Armadillo Flats, Breckinridge, and Chisholm View wind plants with unstable ABL.

For the stable ABL condition, a comparison between the FLORIS TurbOPark King Plains model, and simulations of the Eastern subset of King Plains from AMR-Wind and Nalu-Wind is possible. In the figure below, there is less variation in power production among the individual turbines, resulting in smoother power curves, but a difference can still be seen between the Nalu-Wind and AMR-wind cases.

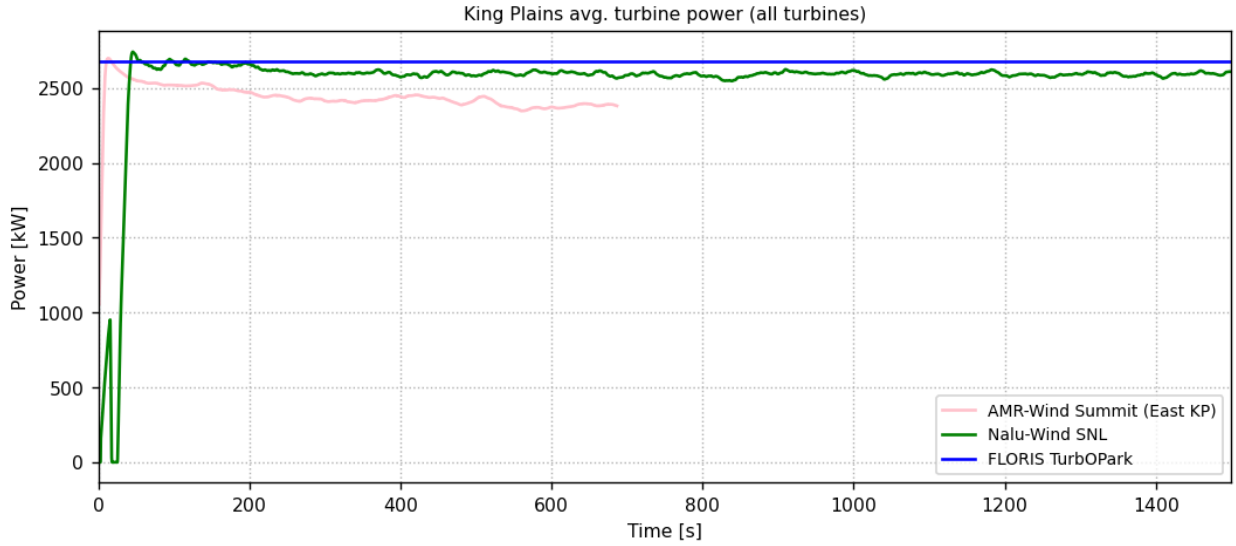

Figure 10. Average power for all turbines in each solver case for the King Plains wind plant with a stable ABL. Each case has a different number of turbines.

Front row power comparison

The observed power differences can be partially explained by differences in the inflow behavior as well as the wake evolution between the various simulations. The difference in wake behavior will be discussed in a subsequent section, but the differences in power production from the inflow alone can be isolated by considering the only front row turbines from King Plains. In the figure below, the averaged power production from the WRF and Nalu-Wind simulations still remains larger than the AMR-Wind simulations for the unstable ABL. For the WRF simulations, this can be explained through the higher hub-height inflow velocity (see Figure 6). However, for the Nalu-Wind simulations, we found that the inflow velocity for the front row turbines from the precursor simulation was also higher than expected (Figure 11). This higher velocity is *not* reflected in the averaged horizontal inflow plane measured far upstream, and suggests that the large scale structures in unstable ABL can greatly impact the wind speed variations in the domain. For the largest AMR-Wind simulation, the local wind speed for the front row turbines remained fairly close to the 9 m/s target, compared to the 9.3 m/s and 9.4 m/s wind speed for Nalu-Wind and WRF. Using a U^3 scaling, this wind speed difference would account for an approximate 10% difference in power production.

The differences in the front row power production for the stable ABL can also be seen in Figure 12 below. Here a small difference in power production still remains, which can also be attributed to a small difference in the local wind speed.

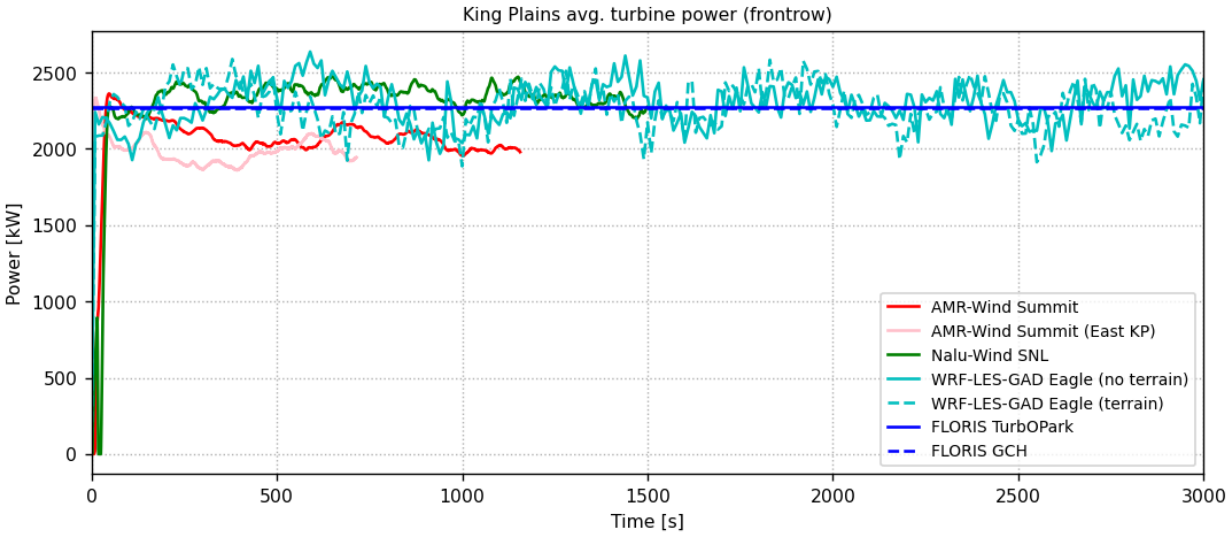

Figure 11. Comparison of the average power for the front row only of King Plains in an unstable ABL.

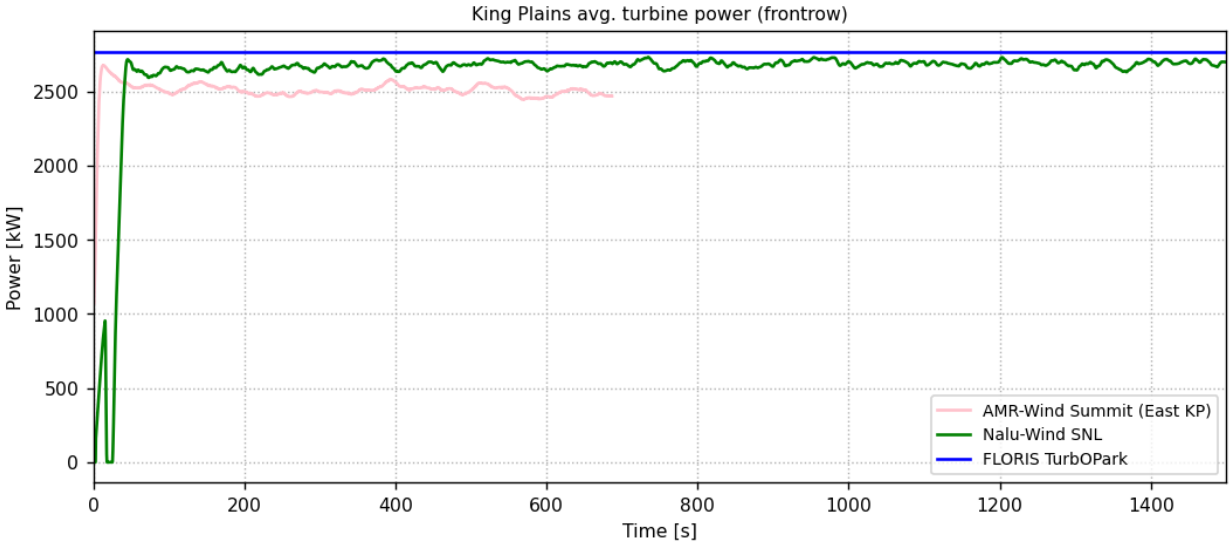

Figure 12. Comparison of the average power for just the front row of King Plains in a stable ABL.

Hub-Height Velocity Contours

Hub-height contours of horizontal velocity are shown below to allow a qualitative comparison between the simulated flow fields. In each case both an instantaneous and an averaged contour is shown.

Unstable ABL

For the unstable ABL condition shown in Figure 13, several immediate differences are apparent. Note that in the FLORIS Gaussian-Curl Hybrid model, the formulation is for a steady-state wake behavior, so the instantaneous and averaged velocity fields are identical. In the simulations where the large scale convective structures were resolved (AMR-Wind, Nalu-Wind, and WRF simulations), the local variations in wind speed and direction are visible in both the instantaneous and the mean velocity fields. These convective structures lead to different inflow velocities for different turbines within the same wind farm, as well as differences in the wake propagation direction. Variations in the local yaw angle were accounted for in the AMR-Wind simulations, but all turbines in the Nalu-Wind simulation have a constant yaw heading of 175 degrees, so yaw misalignment may be present. In the FLORIS model, both the wind speed and direction are constant everywhere, so each turbine is perfectly aligned with the flow.

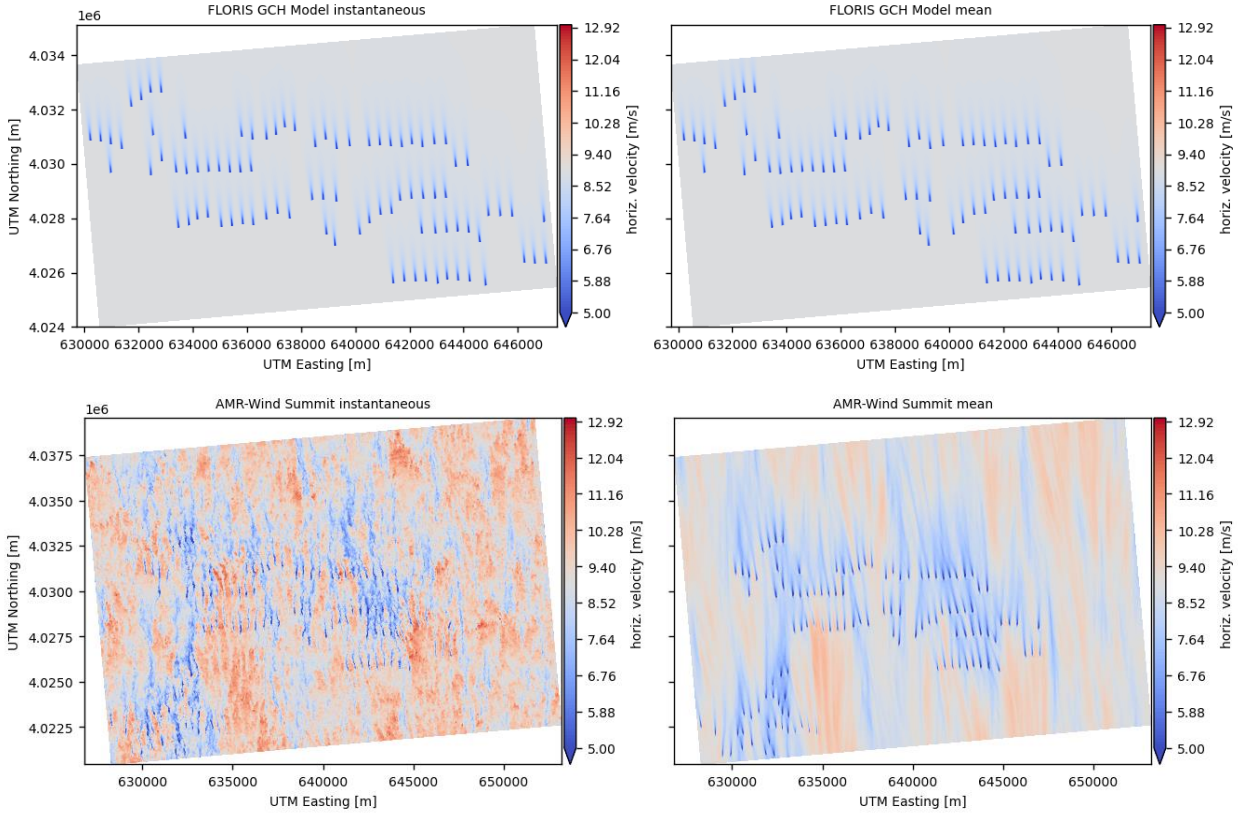

OBJ OBJ

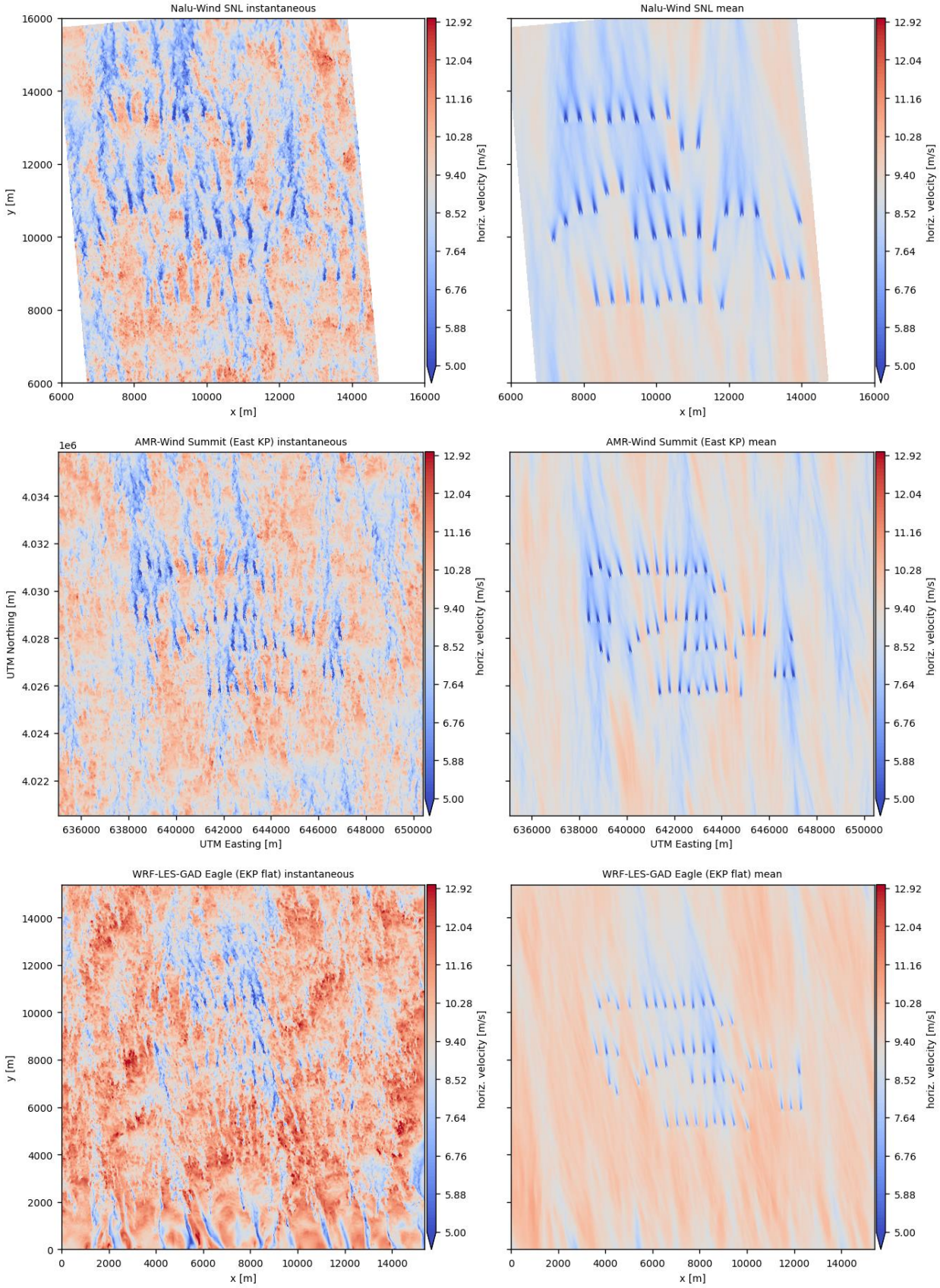
Nalu-Wind SNL instantaneous
Nalu-Wind SNL mean
AMR-Wind Summit (East KP) instantaneous
AMR-Wind Summit (East KP) mean
WRF-LES-GAD Eagle (EKP flat) instantaneous
WRF-LES-GAD Eagle (EKP flat) mean
x [m]
y [m]
UTM Easting [m]
UTM Northing [m]
1e6
horiz. velocity [m/s]
12.92
12.04
11.16
10.28
9.40
8.52
7.64
6.76
5.88
5.00

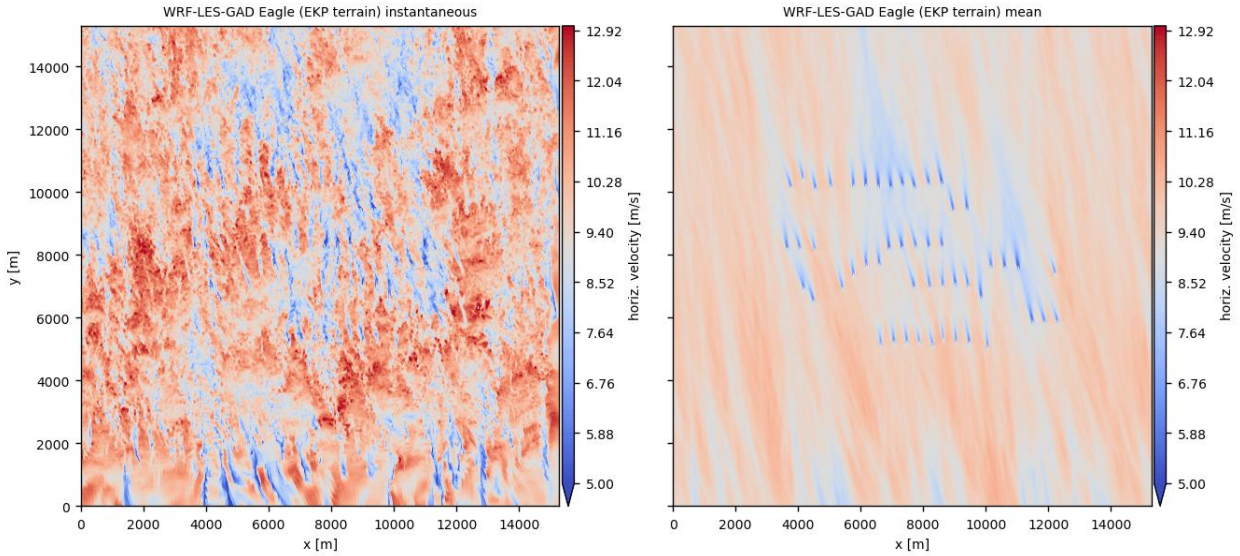

Figure 13. Instantaneous (left) and mean (right) hub height planes for the King Plains wind plant with an unstable ABL for the various solvers (solver identities are annotated as the subplot titles).

Stable ABL

For the stable ABL simulations (Figure 14), the dominant length scales of the turbulent structures are much smaller than for the unstable case, and the resulting velocity fields are much more homogeneous. This leads to much smaller variations in wind speed across the turbines at the King Plains wind farm, and nearly uniform wind directions and wake propagation directions for all turbines.

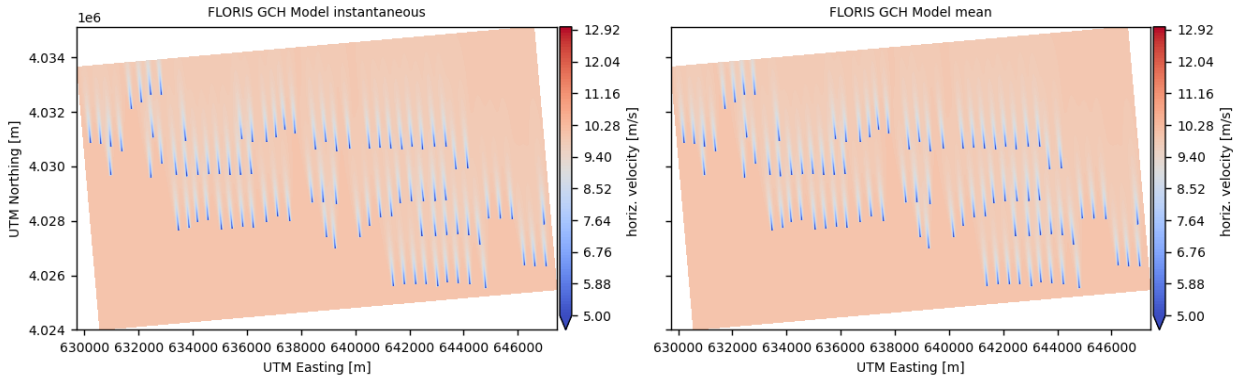

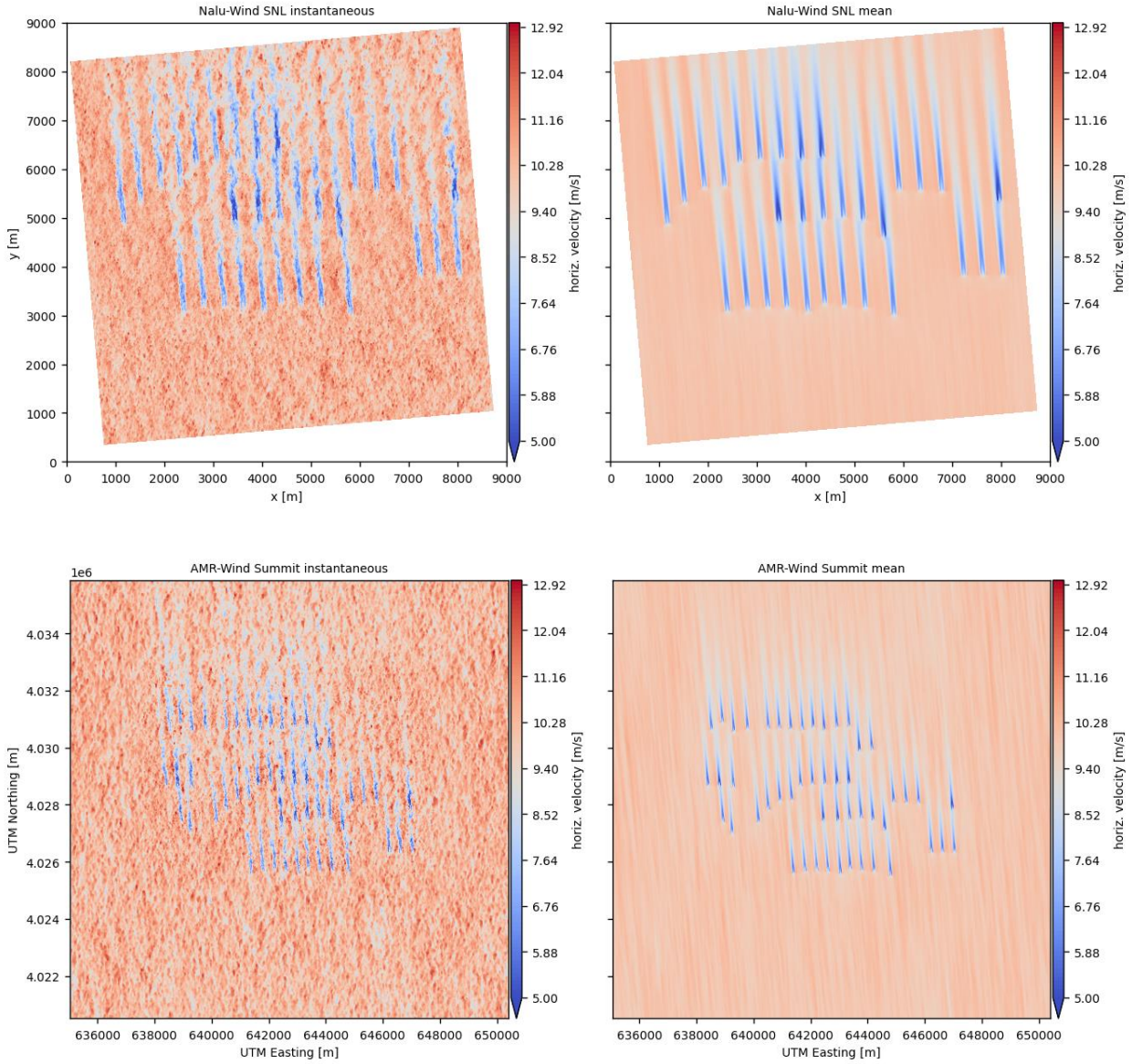

Figure 14. Instantaneous (left) and mean (right) hub height planes for the King Plains wind plant with a stable ABL.

Blockage

Because the AMR-Wind simulations computed both a precursor and turbine flow field using identical parameters, a comparison of the two provides some illustration of the blockage effect. In Figure 15, the ratio of the turbine solution to the precursor solution is shown for the King Plains (stable and unstable ABL) and Thunder Ranch (unstable ABL), and the extent of the upstream velocity slow-down is visible.

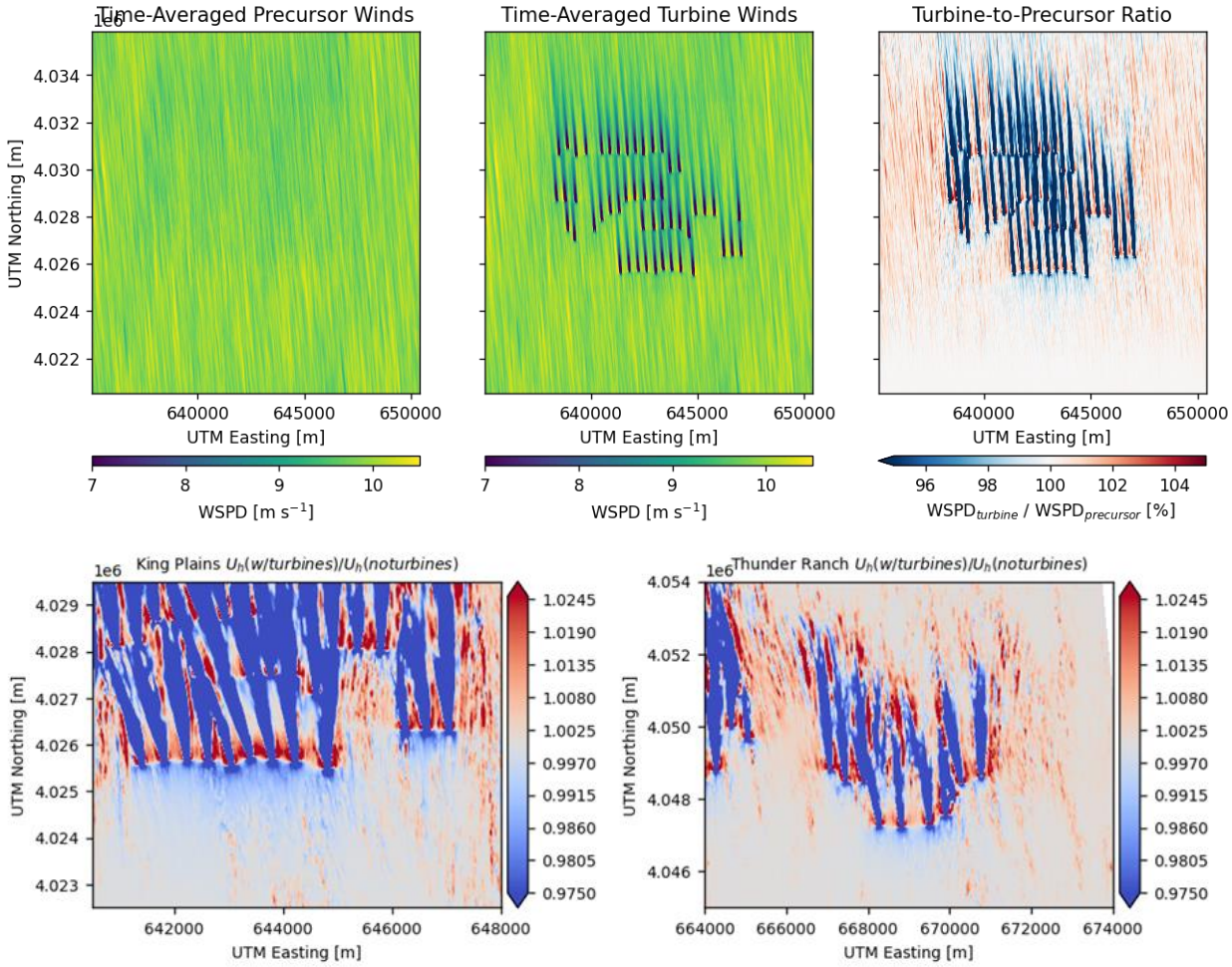

Figure 15. Top row shows the results from AMR-Wind simulations of the eastern King Plains wind plant with a stable ABL. The bottom row shows the AMR-Wind ratio of the turbine/no-turbine simulations for King Plains and Thunder Ranch wind plants with unstable ABL.

Centerline wake velocity

A more quantitative view of the wake behaviors can be seen by examining the averaged turbine centerline velocities for the turbines at King Plains. From each of the simulation models – FLORIS GCH, AMR-Wind, Nalu-Wind, and WRF – the centerline locations on the hub-height plane (following the local wind direction) can be extracted along with the averaged velocity components (Figure 16).

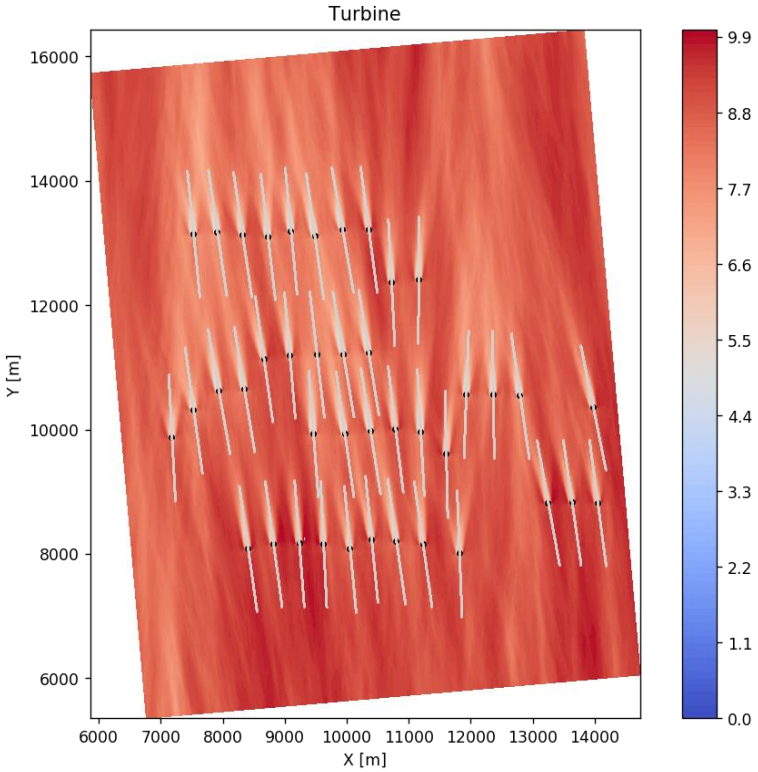

Figure 16. Centerline locations used to compare the wake deficits in the eastern King Plains simulations.

A comparison of the normalized wake velocity on the centerline axis is shown in Figure 17 for the unstable ABL cases. The wake deficits for the WRF-LES-GAD model, both with and without terrain, showed the fastest recovery, followed by the FLORIS GCH model. The microscale LES simulations, Nalu-Wind and AMR-Wind, had the most persistent wakes, with AMR-Wind's wakes being the longest.

Similar comparisons are shown in Figure 18 for the stable ABL case. As expected, the wake recovery was slower compared to the unstable ABL case. The wakes predicted by Nalu-Wind were the most persistent in this set of simulations.

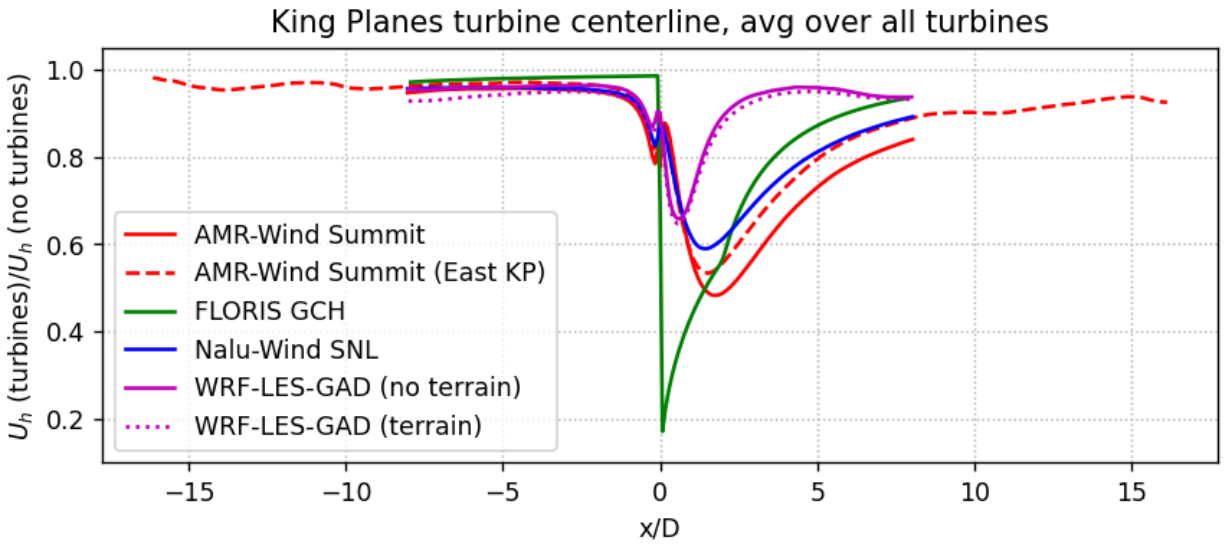

Figure 17. The wake deficit measured along the centerline and averaged for all of the turbines in each simulation for the unstable ABL condition.

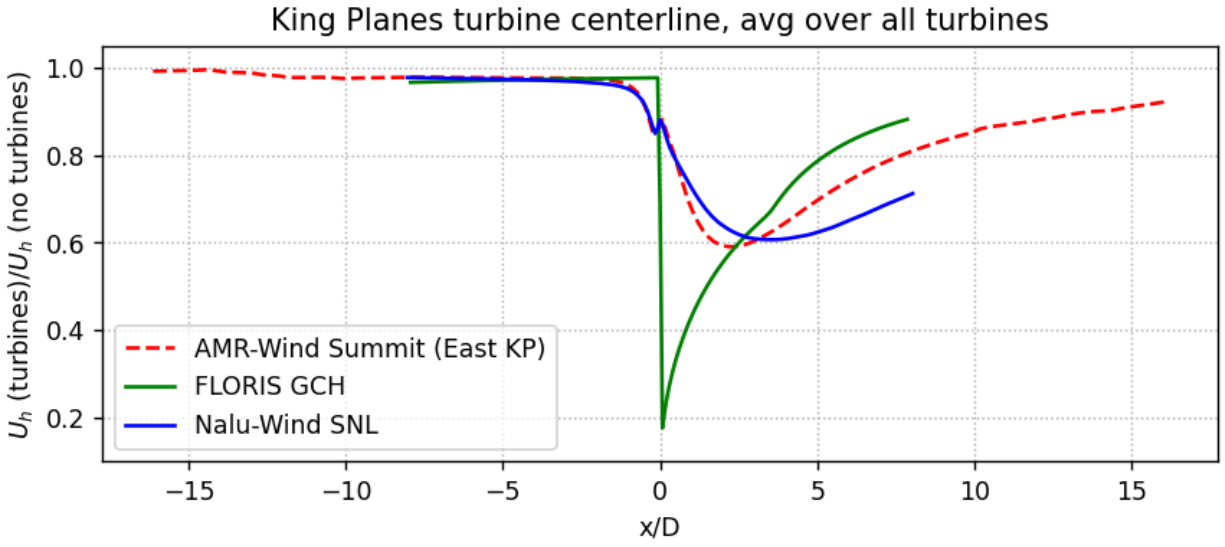

Figure 18. The wake deficit measured along the centerline and averaged for all of the turbines in each simulation for the stable ABL condition.

Front row only comparison

Some additional insight can be gained by examining the wake centerline behavior for just the front row turbines of King Plains. For the unstable ABL case in Figure 19, the differences between the AMR-Wind and Nalu-Wind wakes are still visible. However, we can relate these differences to some variations in the local ambient wind field as well as the ADM turbine models in the codes themselves. As mentioned before, the precursor horizontal velocity in Nalu-Wind at the front row turbines (x/D=0) is noticeably larger compared to AMR-Wind: approximately 9.3

m/s compared to 9.05 m/s for the large scale AMR-Wind calculation. However, there are differences in the observed vertical velocity at the centerline as well. Both the Nalu-Wind and the AMR-Wind (Eastern KP) simulations show a slightly negative vertical velocity, while the large-scale AMR-Wind simulation shows a stronger positive vertical velocity on the centerline. This suggests that the large-scale atmospheric structures may impart a downward or upward motion to the wakes depending on the simulation. Also worth noting is that the ADM implementation in Nalu-Wind neglects the turbine swirl component, so the wakes for AMR-Wind may include more upward motion (Figure 19d).

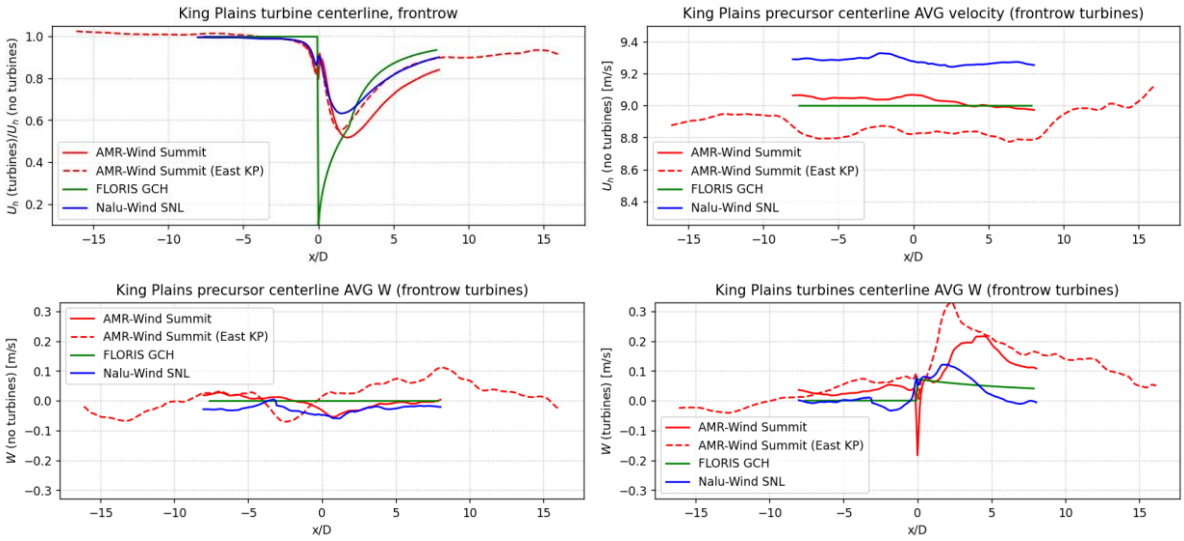

Figure 19. The wake deficit measured along the centerline and averaged for the front row of turbines in each simulation for the unstable ABL condition. The top row shows the horizontal velocity and the bottom row shows the vertical velocity. A comparison of the wind along the same centerline but without the turbines is also shown.

Similar comparisons for the stable ABL case are shown in Figure 20. A small difference in the horizontal velocities at front row turbines is also visible, accounting for some of the power differences. Under stable atmospheric stratification, the precursor velocity field has a negligible vertical velocity component, although the downstream wake still has varying degrees of vertical motion due to the differences in ADM implementation between the AMR-Wind and Nalu-Wind codes.

However, note that because the centerline locations shown in Figure 16 were all extracted along a constant hub-height elevation, any vertical motion in the wake would not be accounted for, and the maximum wake deficit may not be captured in these centerline plots. In future analysis, rotor averaged velocities or wake-following coordinates should be used to more accurately capture the wake behavior.

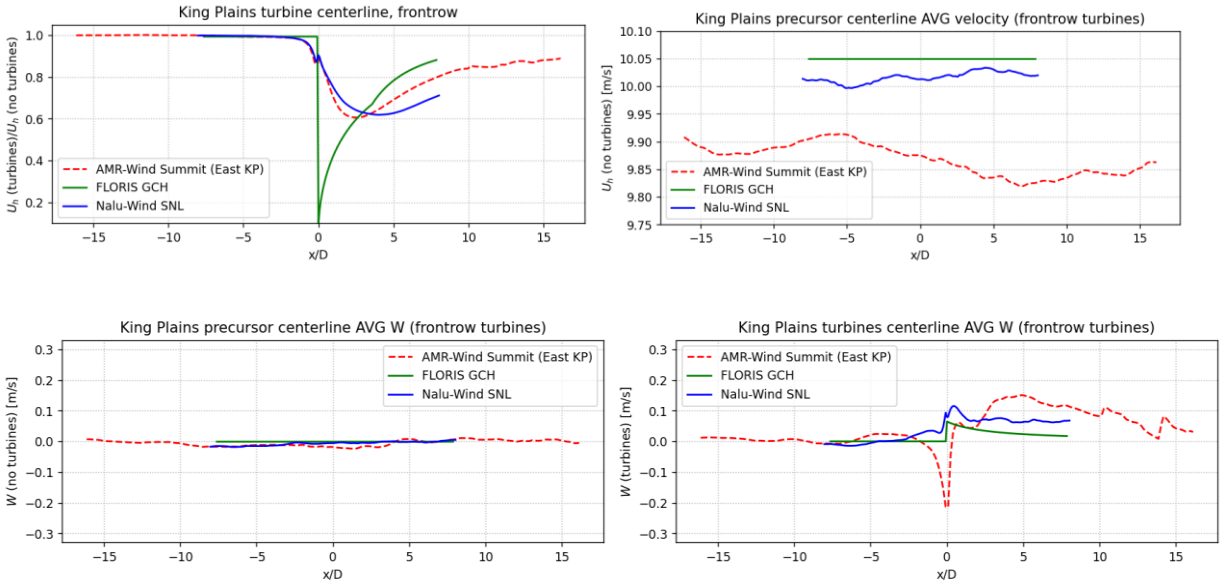

Figure 20. The wake deficit measured along the centerline and averaged for the front row of turbines in each simulation for the stable ABL condition. The top row shows the horizontal velocity and the bottom row shows the vertical velocity. A comparison of the wind along the same centerline but without the turbines is also shown.

Simulated Radar and Lidar

Virtual radar and lidar instruments have been developed to inform the adequacy of the experimental design in AWAKEN to address the science goals. Currently, the radar and lidar are implemented in Nalu-Wind, and work is underway to include them in AMR-Wind, too.

The virtual radar mimics the X-band dual-Doppler radars deployed by Texas Tech University. The approach is:

1. Sample the radar cone with a series of concentric circles along the beam
2. Apply cross-beam weighting with truncated normal halfpower quadrature
3. Interpolate original beamwise velocity distribution to higher resolution (i.e., 1.5 m)
4. Bin the interpolated data on actual radar range resolution (i.e., 15 m)
5. Interpolate the binned data to a Cartesian grid
6. Get horizontal components of velocity with stereo calculation

The scan speed and range are matched to the physical radar instruments, which complete azimuthal sweeps at a series of elevation increments for a return time of ~90 s. The latitudinal and longitudinal position of the radars are also correct relative to the wind farms. One shortcoming of the virtual radar approach, and indeed of all the Nalu-Wind and AMR-Wind simulations, is that topography is ignored. For the virtual radar implementation, we have chosen the radar heights in the LES domain to match the heights of the physical radars relative to the lead turbine in the eastern half of King Plains. The lowest height that the radar can thus sample is 103 m above ground, which is 13 m above hub height for the GE 2.8 machines in King Plains.

The virtual lidar mimics the nacelle-mounted Halo Photonics and Galion lidars that have been furnished for AWAKEN by NREL and EPFL. The approach is:

1. Sample the lidar beam
2. Interpolate original beamwise velocity distribution to higher resolution (i.e., 1.5 m)
3. Bin the interpolated data on actual lidar range resolution (i.e., 30 m)
4. Interpolate the binned data to a Cartesian grid
5. Apply cosine correction to line-of-sight data

The seven different scan patterns deployed at King Plains East are recreated in LES including scans for inflow turbulence, inflow statistics, wake meandering, wake three-dimensional statistics, upstream farm statistics, downstream farm statistics, and speed-up. Return times range from 9.8 s to 295 s. Below in Figure 21, the scanning areas of three of the seven lidars are illustrated.

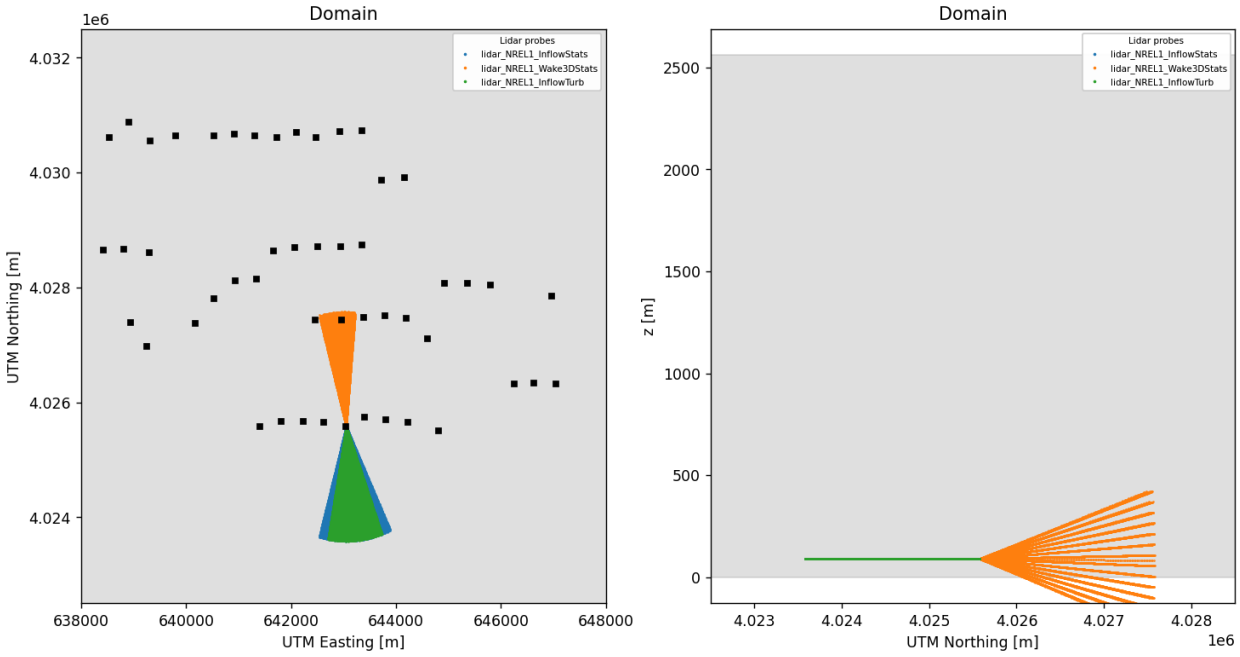

Figure 21. Scanning areas of three of the seven lidar scan patterns.

The figures below provide preliminary results from the virtual instrumentation over the eastern part of King Plains for 10 minutes of the stable atmospheric condition. First, contours of streamwise velocity near hub height are shown. It is apparent that the stable conditions generate clearly defined wakes, which are captured by the virtual instrumentation.

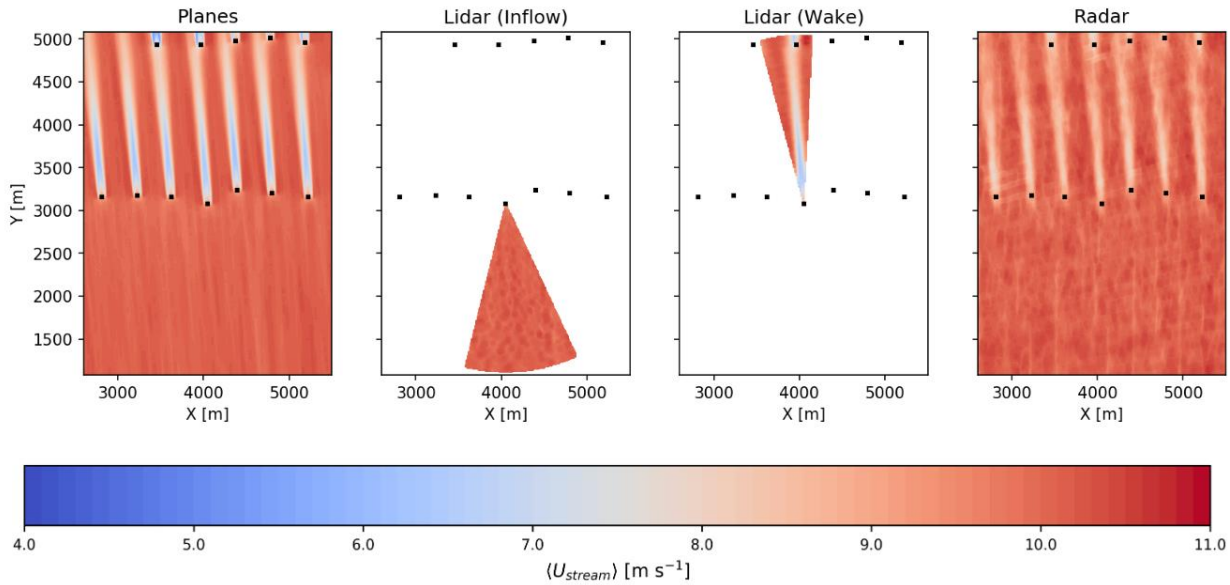

Figure 22. Contours of streamwise velocity near hub-height for the stable ABL condition. The planes and lidar are at a height of 91 m while the radar is at the minimum sampling height of 103 m.

Next in Figure 23 the hub-height wake profile at 8D from the lead turbine is shown (the blue line in the left subplot is the transect that is plotted in the right subplot, and all velocity data is the streamwise component, which has been normalized by the precursor). The lidar results show close agreement with the full planar output except for some overprediction of deficit near the wake edges, where the cosine correction is known to be inaccurate. The radar results show considerable bias versus the planar data, which is a result of the 13 m higher sampling of the radar relative to the planar data as well as the large averaging volume for the radar.

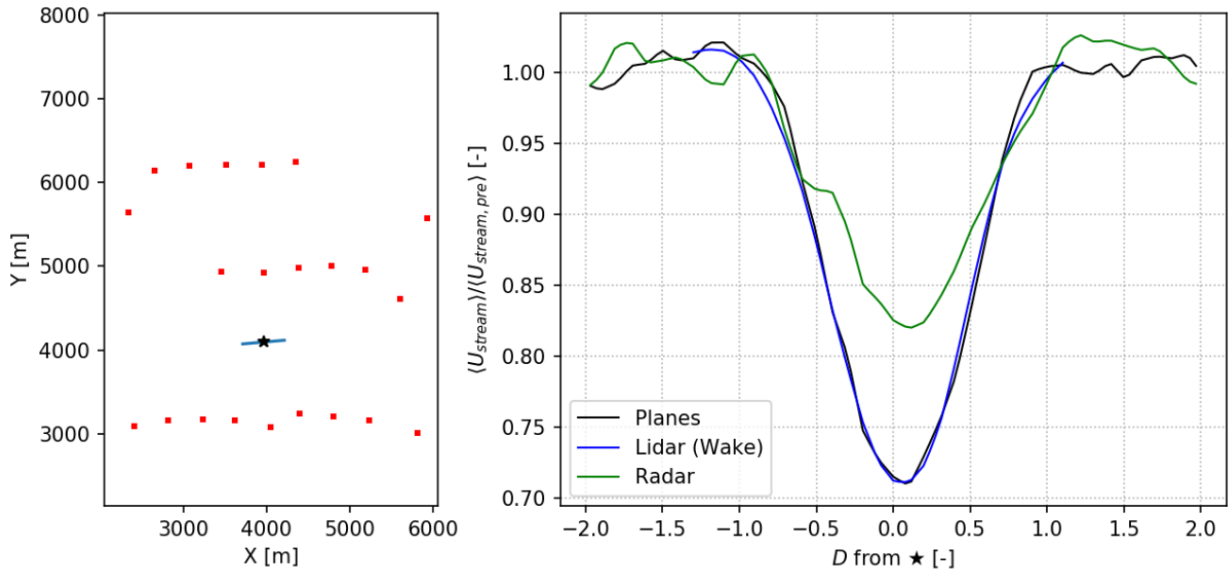

Figure 23. Hub-height wake deficit profile at 8D from the lead turbine. The horizontal axis in the right panel indicates the distance along the blue transect in the left subpanel.

Figure 24 shows the longitudinal hub-height wake deficit where similar observations as above again apply.

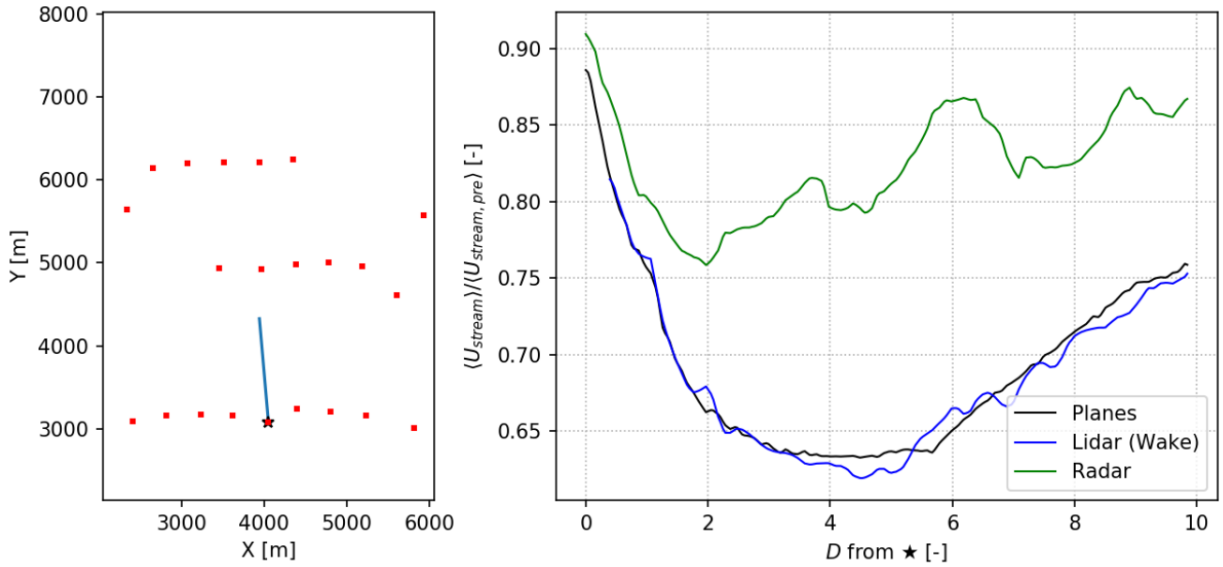

Figure 24. Hub-height wake deficit along the mean wind direction behind the lead turbine.

Figure 25 shows the induction region of the lead turbine. The lidar and radar are capable of qualitatively capturing the induction profile, although statistical convergence of the virtual instruments' results is not reached during the 10 minute simulation because of long return times. For reference, the radar results are an average of just six flow fields, and the lidar results are an average of 21 flow fields.

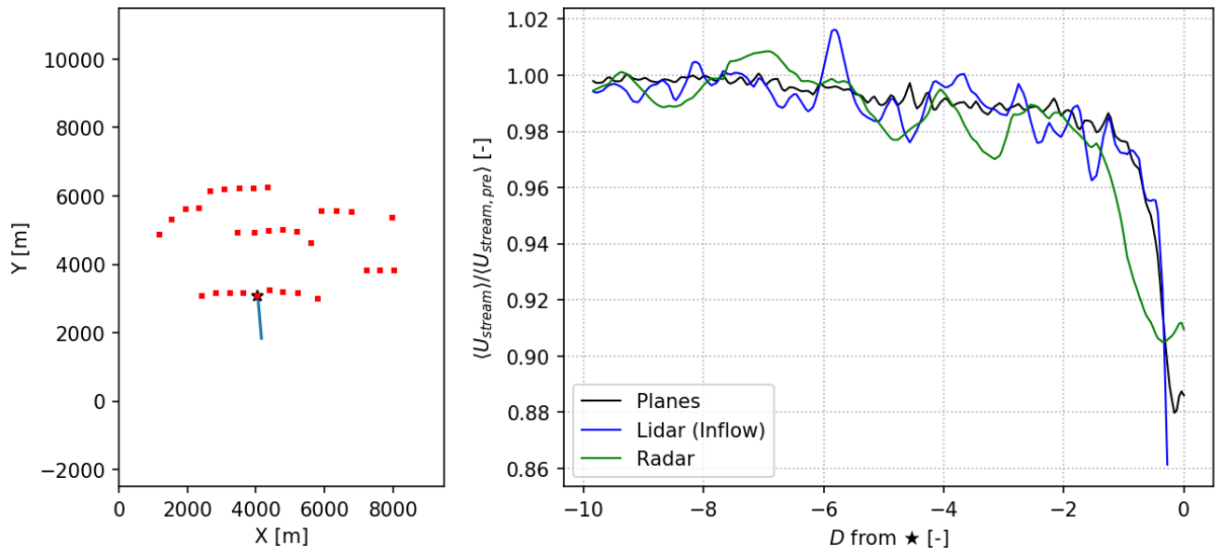

Figure 25. Hub-height induction profiles in front of the lead turbine.

Finally, Figure 26 shows hub-height data along a transect bordering the wind farm, where side-farm blockage may occur. Indeed, the planar data indicates a speed-up effect of up to ~3%. However, the scatter in the radar results make it unlikely that such an effect will be resolvable by the instrument without significantly more sampling time.

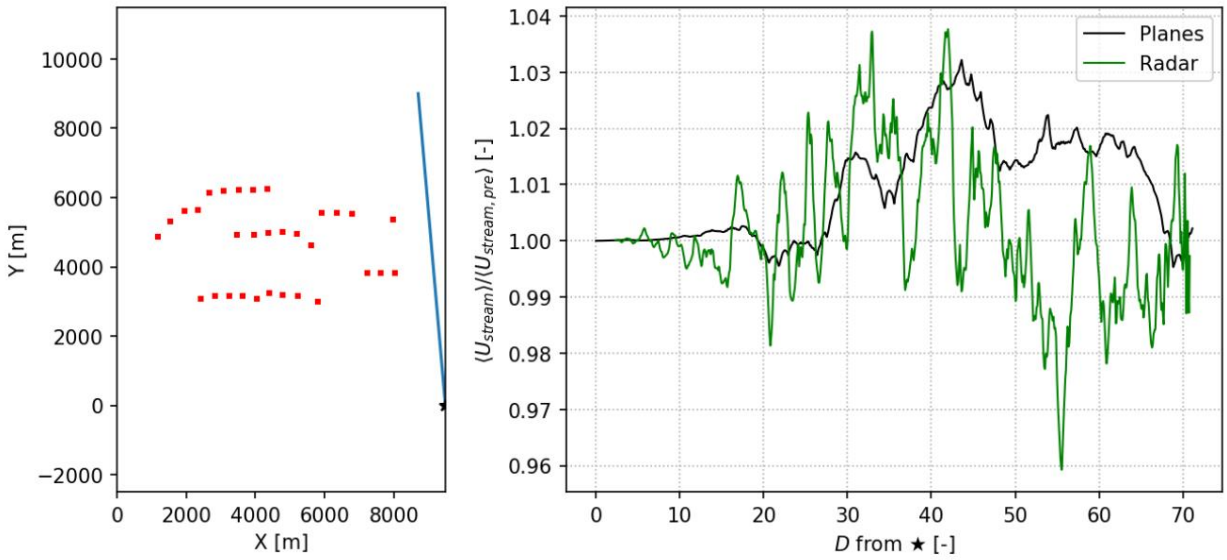

Figure 26. Hub-height blockage profile along a transect bordering the wind farm.

Discussion

Impact of Terrain and Simulated Physics

The Southern Great Plains (SGP) site in Oklahoma was originally selected for the AWAKEN field measurement campaign owing to a number of reasons, one of which is the relatively smooth topography. The goal was to reduce the spatial variability imposed by the topography on the boundary layer winds and turbulence in order to investigate wakes, blockage and farm performance, amongst other things. Thus, here we analyze the role of topography on the spatio-temporal variability of winds, turbulence, and wakes for eastern King Plains simulated with idealized WRF-LES-GAD during convective conditions. The Idealized WRF-LES-GAD simulations are a suitable basis for an assessment of this type, since the four simulated cases only differ by two features: presence or absence of turbines and presence or absence of terrain.

Figure 27 shows the average ratio between hub-height wind speeds of the terrain case to the flat case (*SU = WS_terrain/WS_flat*) for the no-turbine situation to better illustrate and isolate the topographic effects on the flow field. Two distinctive areas are discernible in the speed-up

(SU) map: some patches of wind acceleration (colored red, SU > 1.1) elongated in the along-wind direction are located near the higher ground in the central and western portions of KP. Acceleration is maximum immediately west of the wind farm in an area without turbines in the plot – the real KP wind farm, however, does have turbines operating in that location. The eastern portion of KP is crossed by an area of relatively lower speeds (SU < 0.9) that extends from the domain inlet toward the outlet in the along-wind direction. Turbines in this region will experience lower wind speeds. Despite the absence of site-specific measurements to compare against yet, the topographic acceleration over higher ground and deceleration near lower ground is a well-known feature of wind flow over topography in convection conditions. No simulations have been carried out for the stable case, but the scientific literature on stratified flows over topography indicates that there would be flow field acceleration and deceleration different in character from the convective case. In stable conditions, in the absence of turbines, winds are likely to accelerate descending the slopes and to decelerate ascending the slopes, so that the speed-up map would be different.

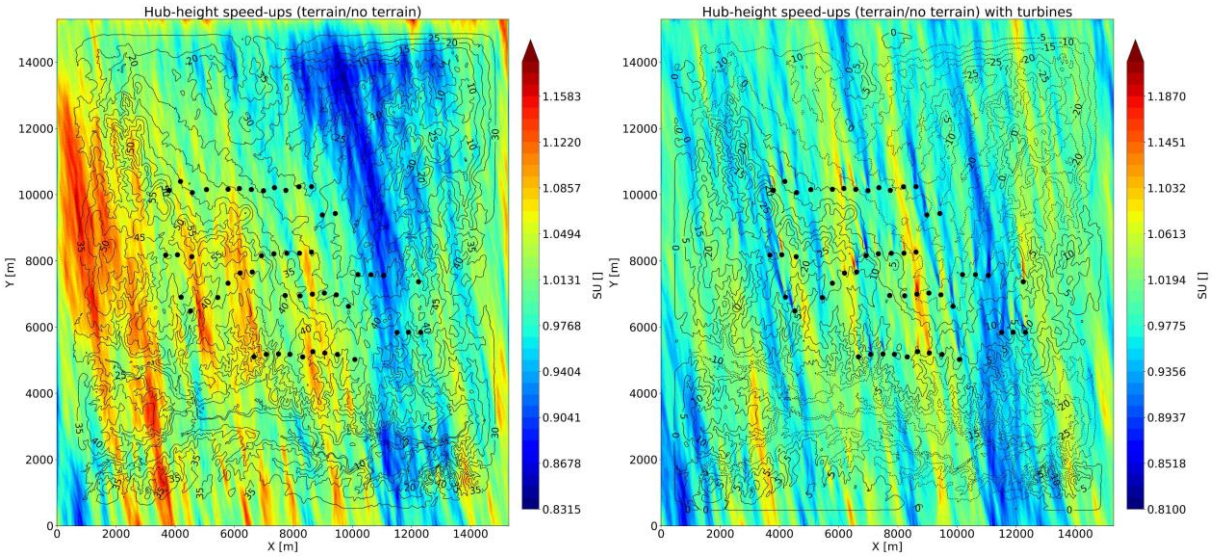

Figure 27. Average hub-height speed-ups obtained as the ratio between the terrain and no terrain cases without turbines (left) and with turbines (right) using WRF-LES-GAD for the convective cases for eastern King Plains (EKP). Wind farm layout is overlaid to highlight which turbine clusters are affected by the spatial variability in the flow field caused by the topography. Terrain contour levels are colored black and some heights are displayed. Terrain elevation was normalized so that the minimum level in the plot is 0 m. The central and western turbines closer to higher ground will benefit from wind acceleration (red areas), whereas those in the eastern side will suffer wind deceleration (blue areas). Despite the mild changes in elevation, these seem sufficient to produce noticeable changes in speed-up. Wake dynamics and turbine performance will be influenced.

Now, the presence of the wind turbines will interact non-linearly with the topographic speed-up field producing a large spatial variability in the wake field (Figure 27, right). The area of reduced wind speeds in the eastern portion of KP for the no-turbine case now interacts with the eastern turbines producing stronger and longer wakes, identifiable as a blue patch stretched in the

along-wind direction. In other parts of the wind farm there is spatial heterogeneity and turbines experience either weaker or stronger wakes because of the topographic effects. Interestingly, it seems that the presence of the wind farm alleviates the spatial variability in the flow field around it and downstream. This is because the formerly strongly red and blue areas for the no-turbine cases (Figure 27, left) have been broken down into smaller and weaker patches of either weaker or stronger wind speeds (Figure 27, right).

In summary, the presence of topography produces a notable influence in the spatio-temporal variability of the flow and wake fields during convective conditions. This effect causes some clusters of turbines to either underperform or outperform, and to produce either shorter and weaker or longer and stronger wakes in comparison with the flat case. The interaction between the topographic speed-up and the turbines seem to break down the flow and turbulence field into smaller patches with heterogeneous speed-ups. Stable conditions have not been simulated, but there is likely to be flow acceleration down the slopes and deceleration up the slopes, thus producing a different speed-up field. On top of that, the role of stable wakes, blockage, and gravity waves should be considered in the future. These effects should be considered when using models that do not account for topographic effects and when planning and executing field measurements in the AWAKEN project.

Next steps

The first efforts to follow on the preparation of this summary will be a deeper analysis of differences across the models to learn where any model implementation errors may have occurred, to improve post-processing procedures to maximize consistency in the way each model's predictions are characterized, and to refine the selection of quantities of interest for comparing across models. These results will also inform what inflow conditions and wind turbine/wind farm configurations should be focused on for the next simulations. The large-domain stable AMR-Wind case will be run in the near future with the inclusion of the radar and lidar sampling to capture the farm-to-farm interactions. An analysis of the simulation plane sampling to the lidar and radar sampling will help inform our ability to capture the testable hypothesis, and the post-processing workflow will be developed for both the simulation and field test observations to help with comparisons and the development of benchmarks for the Q4 milestone. Another proposed idea will be to use the LES models to look at the effects of wind plant control on the simulated observations for comparison with field test observations.

Acknowledgements

Sandia National Laboratories is a multimission laboratory managed and operated by National Technology & Engineering Solutions of Sandia, LLC, a wholly owned subsidiary of Honeywell International Inc., for the U.S. Department of Energy's National Nuclear Security Administration under contract DE-NA0003525. The views expressed in the article do not necessarily represent the views of the U.S. Department of Energy or the United States Government. This work was

accomplished through funding from the U.S. Department of Energy Wind Energy Technologies Office.

This research used resources of the Oak Ridge Leadership Computing Facility, which is a DOE Office of Science User Facility supported under Contract DE-AC05-00OR22725, which was provided through the ASCR Leadership Computing Challenge (ALCC) program.

References

Almgren, A. S., J. B. Bell, P. Colella, L. H. Howell and M. L. Welcome, "A conservative adaptive projection method for the variable density incompressible Navier--Stokes equations," Journal of Computational Physics, vol. 142, no. 1, pp. 1-46, 1998.

Deardorff, J. W. (1980). Stratocumulus-capped mixed layers derived from a three-dimensional model. *Boundary-Layer Meteorology*, *18*(4), 495–527. https://doi.org/10.1007/BF00119502

Domino, S. P. "Sierra Low Mach Module: Nalu Theory Manual 1.0" Sandia National Laboratories Unclassified Unlimited Release (UUR) In: SAND2015-3107W, (2015), Available: https://github.com/NaluCFD/NaluDoc.

Kosović, B. (1997). Subgrid-scale modelling for the large-eddy simulation of high-Reynolds-number boundary layers. *Journal of Fluid Mechanics*, *336*, 151–182. https://doi.org/10.1017/S0022112096004697

Mirocha, J. D., Kosovic, B., Aitken, M. L., & Lundquist, J. K. (2014). Implementation of a generalized actuator disk wind turbine model into the weather research and forecasting model for large-eddy simulation applications. *Journal of Renewable and Sustainable Energy*, *6*(1). https://doi.org/10.1063/1.4861061

Moeng, C.H. "A large-eddy-simulation model for the study of planetary boundary-layer turbulence," Journal of the Atmospheric Sciences, vol. 41, no. 13, pp. 2052-2062, 1984.

Muñoz-Esparza, D., Kosovic, B., van Beeck, J., & Mirocha, J. (2015). A stochastic perturbation method to generate inflow turbulence in large-eddy simulation models: Application to neutrally stratified atmospheric boundary layers. *Physics of Fluids*, *27*(3). https://doi.org/10.1063/1.4913572

NWTC Information Portal (OpenFAST). URL: https://nwtc.nrel.gov/OpenFAST.

Skamarock, W. C., Klemp, J. B., Dudhi, J., Gill, D. O., Barker, D. M., Duda, M. G., Huang, X.-Y., Wang, W., & Powers, J. G. (2019). A Description of the Advanced Research WRF Version 4. *Technical Report*, *June*, 113. https://doi.org/10.5065/D6DZ069T

Sprague, M., Ananthan, S., Vijayakumar, G., and Robinson, M., 2020. “Exawind: A multi-fidelity modeling and simulation environment for wind energy”. In Journal of Physics: Conference Series, IOP Publishing.

Sverdrup, K., N. Nikiforakis and A. Almgren, "Highly parallelisable simulations of time-dependent viscoplastic fluid flow with structured adaptive mesh refinement," Physics of Fluids, vol. 30, no. 9, p. 093102, 2018.

Vasaturo, R., Kalkman, I., Blocken, B., and van Wesemael, P. J. V., 2018. “Large eddy simulation of the neutral atmospheric boundary layer: performance evaluation of three inflow methods for terrains with different roughness”. Journal of Wind Engineering and Industrial Aerodynamics, 173, pp. 241–261.

Yoshizawa, A., and Horiuti, K., 1985. “A statistically derived subgrid-scale kinetic energy model for the large-eddy simulation of turbulent flows”. Journal of the Physical Society of Japan, 54(8), pp. 2834–2839.